



OPEN ACCESS

EDITED BY

Amrishi Kumar Srivastava,
Deen Dayal Upadhyay Gorakhpur
University, India

REVIEWED BY

Jinwoo Park,
University of Seoul, South Korea
Dipendra Sharma,
Deen Dayal Upadhyay Gorakhpur
University, India

*CORRESPONDENCE

Zacharias G. Fthenakis,
fthenak@eie.gr

SPECIALTY SECTION

This article was submitted to Physical
Chemistry and Chemical Physics,
a section of the journal
Frontiers in Chemistry

RECEIVED 23 May 2022

ACCEPTED 29 July 2022

PUBLISHED 29 August 2022

CITATION

Fthenakis ZG, Petsalakis ID, Tozzini V
and Lathiotakis NN (2022), Evaluating
the performance of ReaxFF potentials
for sp^2 carbon systems (graphene,
carbon nanotubes, fullerenes) and a
new ReaxFF potential.
Front. Chem. 10:951261.
doi: 10.3389/fchem.2022.951261

COPYRIGHT

© 2022 Fthenakis, Petsalakis, Tozzini
and Lathiotakis. This is an open-access
article distributed under the terms of the
[Creative Commons Attribution License
\(CC BY\)](https://creativecommons.org/licenses/by/4.0/). The use, distribution or
reproduction in other forums is
permitted, provided the original
author(s) and the copyright owner(s) are
credited and that the original
publication in this journal is cited, in
accordance with accepted academic
practice. No use, distribution or
reproduction is permitted which does
not comply with these terms.

Evaluating the performance of ReaxFF potentials for sp^2 carbon systems (graphene, carbon nanotubes, fullerenes) and a new ReaxFF potential

Zacharias G. Fthenakis^{1,2,3,4,5*}, Ioannis D. Petsalakis²,
Valentina Tozzini^{1,5} and Nektarios N. Lathiotakis²

¹Istituto Nanoscienze-CNR, Pisa, Italy, ²Theoretical and Physical Chemistry Institute, National Hellenic Research Foundation, Athens, Greece, ³Department of Surveying and Geoinformatics Engineering, University of West Attica, Athens, Greece, ⁴Department of Marine Engineering, University of West Attica, Athens, Greece, ⁵NEST, Scuola Normale Superiore, Pisa, Italy

We study the performance of eleven reactive force fields (ReaxFF), which can be used to study sp^2 carbon systems. Among them a new hybrid ReaxFF is proposed combining two others and introducing two different types of C atoms. The advantages of that potential are discussed. We analyze the behavior of ReaxFFs with respect to 1) the structural and mechanical properties of graphene, its response to strain and phonon dispersion relation; 2) the energetics of $(n, 0)$ and (n, n) carbon nanotubes (CNTs), their mechanical properties and response to strain up to fracture; 3) the energetics of the icosahedral C_{60} fullerene and the 40 C_{40} fullerene isomers. Seven of them provide not very realistic predictions for graphene, which made us focusing on the remaining, which provide reasonable results for 1) the structure, energy and phonon band structure of graphene, 2) the energetics of CNTs versus their diameter and 3) the energy of C_{60} and the trend of the energy of the C_{40} fullerene isomers versus their pentagon adjacencies, in accordance with density functional theory (DFT) calculations and/or experimental data. Moreover, the predicted fracture strain, ultimate tensile strength and strain values of CNTs are inside the range of experimental values, although overestimated with respect to DFT. However, they underestimate the Young's modulus, overestimate the Poisson's ratio of both graphene and CNTs and they display anomalous behavior of the stress - strain and Poisson's ratio - strain curves, whose origin needs further investigation.

KEYWORDS

ReaxFF, graphene, nanotubes, fullerenes, energetics, mechanical properties, phonon band structure

1 Introduction

The isolation of graphene, 2 decades ago (Novoselov et al. (2004)) provided a new material with extremely interesting and unique properties, both from the scientific and the technological point of view. Graphene is not only the first two-dimensional (2D) material, but it also has unique properties including (among others) the linear bands at the Fermi level (Castro Neto et al. (2009)), the large Young's modulus (Fthenakis and Lathiotakis (2015)) and thermal conductivity (Berber et al. (2000); Fthenakis and Tománek (2012); Fthenakis et al. (2014)). Moreover, some of those properties are shared with several three-fold coordinated carbon structures, which can be considered as graphene derivatives, e.g. carbon nanotubes (Iijima (1991)), fullerenes (Kroto et al. (1985)), haeckelites (pentaheptites (Terrones et al. (2000); Fthenakis and Lathiotakis (2015); Crespi et al. (1996)), tetraoctites (Liu et al. (2012); Sheng et al. (2012); Fthenakis and Lathiotakis (2015)), or even three-dimensional structures (Côté et al. (1998); Liu and Cohen (1992); Fthenakis (2016)), foams (Zhu et al. (2014); Inagaki et al. (2015); Liu et al. (2020); Bellucci and Tozzini (2020)), honeycombs (Fthenakis (2017); Krainyukova and Zubarev (2016)), which also attracted a lot of interest.

Several theoretical and computational studies have been devoted to those systems (Bellucci and Tozzini (2020); Berber et al. (2000); Castro Neto et al. (2009); Côté et al. (1998); Crespi et al. (1996); Fthenakis (2016, 2017); Fthenakis and Lathiotakis (2015); Fthenakis and Tománek (2012); Fthenakis et al. (2014); Liu and Cohen (1992); Liu et al. (2012); Terrones et al. (2000); Zhu et al. (2014)). Depending on the size, more or less accurate methods are appropriate. For relatively small systems (up to hundreds of atoms¹), the more accurate, but more computationally demanding *ab initio* methods, can be used. For larger systems, however, these become practically unfeasible to be performed and therefore less time consuming methods should be used. Semi-empirical methods using parameterized approximations for the superposition integrals (Elstner et al. (1998); Lathiotakis et al. (1996); Fthenakis et al. (2003); Hoffmann (1963)) can apply up to thousands of atoms. For even larger systems, one must abandon the explicit quantum description of electronic structure and adopt classical potentials, also called "Force Fields" (FF), implicitly including the effect of electrons. These potentials are usually analytic expressions of the energy of the system as a function of the internal coordinates, with parameters fitted onto *ab initio* calculations or based on experimental data of different origin (Schuler et al. (2001); Weiner et al. (1984, 1986)). Since the parameterization is typically optimized based on a given set of configurations and/or in given chemical-physical conditions, its interpolation

or extrapolation in different situations implies possible inaccuracies raising the well-known problem of the FF transferability.

Historically, the first attempt to develop a classical potential for carbon lead to the Tersoff potential (Tersoff (1988)). Its analytical form (Abell (1985)) describes the dependence of the interaction on the bond order (BO), allowing the treatment of different carbon allotropes (Berber et al. (2000); Fthenakis and Tománek (2012); Fthenakis et al. (2014); Zhao et al. (2019); Ng et al. (2013)). Similar potentials were subsequently proposed, by Chelikowsky (Chelikowsky (1992)), Khor–Das Sharma (Khor and Das Sarma (1988)) and Takai *et al.* (Takai et al. (1990)). Moreover, different parameterizations of the original Tersoff potential were developed attempting to provide a more accurate description of phonon dispersion relation (Lindsay and Broido (2010)) and mechanical properties (Rajasekaran et al. (2016)) in graphene and diamond (Shi et al. (2021)). Subsequently, a new version of the Tersoff potential was suggested by Brenner (Brenner (1990)) to extend the FF to hydrocarbons, improve the description of conjugation and sp² and sp³ bonds.

The potentials described so far, may be considered as the first generation of BO potentials (BOPs). The second generation includes the so called "Reactive Empirical Bond Order" (REBO) potentials REBO-I (Brenner et al. (2002)) and REBO-II (Pastewka et al. (2008)). In these, the BO is described in terms of $\sigma - \pi$ and π contributions, allowing the description of covalent intramolecular bonding, breaking and formation, and including dihedral angle torsional interactions. Several such potentials have been developed to represent elements beside carbon, e.g. S and H (Beardmore and Smith (1996); Dyson and Smith (1996)), or O and H (Ni et al. (2004); Fonseca et al. (2011)) or F and H (Jang and Sinnott (2004)). One issue of these potentials is the poor representation of the van der Waals (vdW) forces, preventing the description of inter-molecular interactions. The so called "Long range Carbon Bond Order Potentials" (LCBOPs) were therefore developed, available in two subsequently improved versions LCBOP-I (Los and Fasolino (2003)) and LCBOP-II (Los et al. (2005)). With the same aim, the so called "Adaptive Intermolecular Reactive Empirical Bond Order (AIREBO)" potentials (Stuart et al. (2000)) and AIREBO(-M) (O'Connor et al. (2015)) were developed.

A different approach is adopted in the class of molecular mechanics FFs (MM-FFs), characterized by a distinction between bonded and non bonded terms of the interactions, implying that the chemical connectivity, or topology, must be given as an input in the model. As a consequence, the energy can be written as a sum of energy contributions from bond stretching, bond angle bending, proper and improper dihedral angle torsion terms, i.e., the chemical or bonding terms assigned based on the given topology, plus terms describing van der Waals interactions and electrostatics. With respect to BOPs and reactive FFs, these are much simpler concerning the analytical

¹ For routine runs workstations. Thousands on High Performance Computing systems.

forms and implementation, more numerically robust and, up to two orders of magnitude computationally cheaper. On the other hand, they are a step lower in the scale of transferability, requiring different sets of parameters optimized for different cases. For this reason, many different such FF have been developed. A non exhaustive list includes: MM2 (Allinger (1977)), MM3 (Allinger et al. (1989)) and MM4 (Allinger et al. (1996)) for hydrocarbons, the universal FFs UFF (Rappe et al. (1992)) and COMPASS (Sun (1998)), and those specialized for bio-molecules, such as Amber (Weiner et al. (1984; 1986)), CHARMM (Brooks et al. (1983); Nilsson and Karplus (1986)), DREIDING (Mayo et al. (1990)), GROMOS (Schuler et al. (2001)). A potential of that category has been also developed by Fthenakis et al. (Fthenakis et al. (2017); Chatzidakis et al. (2018); Kalosakas et al. (2013, 2021)) for the description of three-fold coordinated carbon systems. The main drawback of these FFs is their inability to describe chemical reactions.

Aiming to fix this problem, the group of Van Duin provided new ideas resulting in the ReaxFF potentials (van Duin et al. (2001)), which can be considered as an evolution of the BOPs and are now the state-of-the-art potentials to reproduce reactivity. Indeed, their (large number of) parameters are fitted to a large training set of atomic arrangements in the configuration space provided by *ab initio* simulations, which include also reactive chemical conditions. To the best of our knowledge, the FFs belonging to the ReaxFF class developed for C and other elements are:

- 1) RDX (Strachan et al. (2003)), originally developed to study the chemistry of nitramine explosions
- 2) CHO-2008 (Chenoweth et al. (2008)), for the combustion of hydrocarbons
- 3) Budzien potential (Budzien et al. (2009)), including interactions between C, N, O and H
- 4) Mattsson potential (Mattsson et al. (2010)), including interactions between C, O and H
- 5) CHON-2010 (Kamat et al. (2010)), developed to study the formation of soot particles and their interactions with several substances including noble gases
- 6) The low gradient (lg) potential (Liu et al. (2011)), an extension of the RDX potential including London dispersion terms
- 7) The charge-implicit ci-CH (Kański et al. (2018)) potential for hydrocarbons improved in terms of computational cost
- 8) C-2013 (Srinivasan et al. (2015)) for carbon condensed phases
- 9) CHO-2016 (Ashraf and van Duin (2017))–CHON-2019 (Kowalik et al. (2019)), subsequent improvements of CHO-2008 including C parameters from C-2013 and parameters for N, for simulations of (bio) polymers

Although (on general grounds) ReaxFFs are more accurate than BOPs and more general than MM-FFs, the earlier ReaxFF potentials still suffered from transferability problems, being

trained on specific systems and under specific conditions. The subsequent evolution brings improvements in this respect: C-2013 was developed to replace CHO-2008 for the study of carbon condensed phases (Jensen et al. (2015); Srinivasan et al. (2015)), while CHO-2016 was aimed at improving the performances on small hydrocarbons (Ashraf and van Duin (2017)).

Here, we test the performance of the above mentioned ReaxFFs, i.e. potentials (1)–(9) and GR-RDX-2021, on graphene and other sp^2 carbon systems (nanotubes and fullerenes) as a first step for the evaluation of their adequacy to be used in the study of interactions between these systems and other molecules, which is the focus of a forthcoming paper. In detail, we study: 1) the structural, energetic and mechanical properties of graphene, its response to strain and phonon dispersion, 2) the structural, energetic and mechanical properties of $(n, 0)$ and (n, n) carbon nanotubes (CNTs), and their response to strain up to the fracture limit and 3) the structural and energetic properties of the 40 C_{40} fullerene isomers and the icosahedral C_{60} , examining the predictions of the considered potentials with respect to the pentagon adjacency penalty rule. Seven of those potentials predict a Poisson's ratio value near to unit. Such an unphysical value affect significantly the mechanical or thermal deformations of graphene. We therefore focus on the remaining potentials, namely, C-2013, CHO-2016/CHON-2109 and we propose a new one, called GR-RDX-2021, which is a combination of the C-2013 and RDX potentials with improved accuracy obtained by a limited reintroduction of the concept of atom type.

2 Methods

2.1 Model systems and general setup

Simulations and calculations were performed with the software LAMMPS (Thompson et al. (2022)). Periodic boundary conditions were applied using the natural periodicity in xy direction for graphene, and z for nanotubes. In the other directions and for fullerenes, we left gaps of free space of at least 100 Å, to avoid interactions between periodic images. Specifically:

- **graphene:** we used rectangular supercell built by the 12×21 repetition of the rectangular 4-atom unit cell along the xy -plane (see Figure 1A, the supercell includes 1,008 atoms).
- **CNTs:** we considered single wall CNTs with $(n, 0)$ and (n, n) chiralities ($n = 1-100$ for $(n, 0)$ CNTs and $n = 1-20$ for (n, n)), at different values of the strain along the axis. The supercells were built by repeating 10 $4n$ -atom unit cells.
- **Fullerenes:** we focused on the icosahedral C_{60} and the 40 C_{40} isomers, corresponding to all possible arrangements

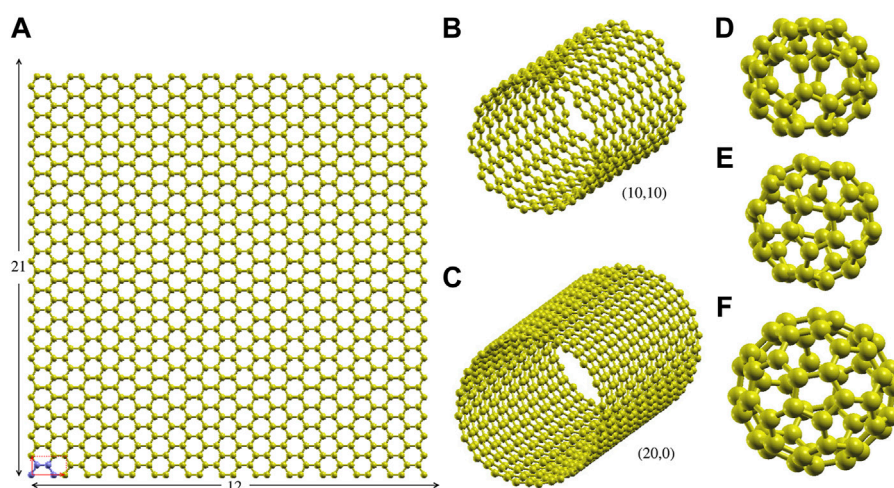


FIGURE 1

Supercells and representative structures. **(A)** The 1,008 atom 12×21 graphene rectangular supercell (size $\approx 51.12 \text{ \AA} \times 51.65 \text{ \AA}$). The 4-atom rectangular unit cell is shown in the left down corner of the structure (red rectangle). **(B)** and **(C)** The supercell of the (10,10) and (20,0) carbon nanotubes, as representatives of the (n, n) and $(n, 0)$ nanotubes. **(D)**, **(E)** The no. 38 and 39 C_{40} fullerene isomers, as representatives of the 40 C_{40} fullerene isomers. **(F)** The icosahedral C_{60} fullerene.

of pentagonal and hexagonal rings (Fowler and Manolopoulos (1995)).

To calculate the response to strain, structure relaxations are performed at fixed strain using a grid of equidistant strain values along x and y directions for graphene (arm chair and zig-zag) and along z for CNTs. The convergence criteria were set at 10^{-6} kcal/(mole \AA) ($\approx 4 \times 10^{-8}$ eV/ \AA) for the forces on atoms and 10^{-4} kcal/mol (or 4×10^{-9} eV/atom) for the global energy variation. The Young's modulus E and the Poisson's ratio ν are calculated using the dependence of energy on strain and correlation between strain components. Phonon dispersion relations in graphene are calculated evaluating the forces for given structural distortions ("frozen phonon" method), as described in the corresponding sections, where additional details of the calculations are reported.

2.2 A new hybrid ReaxFF

As it will be shown in the next sections, most of the ReaxFF potentials predict an unrealistic value of ν . The solution to this problem might follow the strategy of the generalization of ReaxFFs by training on extended systems, as for the recently developed CHON-2019 potential (Kowalik et al. (2019)), which requires, however, a dedicated effort. In this work, we obtain similar performances in terms of both mechanical properties and reactivity towards organic molecules with a simpler approach based on the combination of previous ReaxFF potentials without

reparameterizing them. Specifically we combined C-2013 (Srinivasan et al. (2015)), for the interactions between three-fold coordinated carbons in graphene, with RDX (Strachan et al. (2003)), for all other interactions, within a hybrid new potential that we call *GR-RDX-2021*. This will incorporate the good mechanical properties of C-2013, developed for extended sp^2 systems, and of RDX developed to describe interactions between C, H, N and O.

To follow this idea, 2 C atoms types are defined: those belonging to graphene (or other three-fold coordinated carbon systems) and all others. Denoting the former as " C_g " and the latter as " C ", one has three kinds of carbon-carbon interactions, namely C_g - C_g , C_g - C and C - C , and three kinds of interaction with other elements (E), namely C_g -E, C -E and E-E. In *GR-RDX-2021*, C_g - C_g are described by C-2013, and C - C , C -E, E-E by RDX. C_g - C and C - C interactions are equivalent, as well as, C_g -E and C -E.

ReaxFF potentials have two groups of parameters. The first includes some general ones, e.g. those related to the description of the switch function, same for all interactions. The second group contains those describing the element dependent 2-, 3- and 4-body interactions. As C-2013 and RDX have different parameters of the first group, we chose those from the RDX for the hybrid potential. This means that for interactions of C, H, O, N, and of them with C_g , it behaves as in RDX, while for the C_g - C_g behaves as a modified C-2013. The general performance of the new potential specifically regarding C_g - C and C_g -E interactions must also be tested, which is the matter of a forthcoming paper. It is worth noting that *GR-RDX-2021* is intrinsically capable of representing the sp^2 - sp^3 and sp^3 interactions,

TABLE 1 Predictions of the ReaxFF potentials considered in the present study for the structural, energetic and mechanical properties of graphene. 1) Cohesive energy U_{coh} , and 2) bond length a_0 of the optimum energetically graphene structure, 3) Young's modulus $E_x = \sigma_{xx}/\epsilon_{xx}$ and 4) Poisson's ratio $\nu_x = -\epsilon_{yy}/\epsilon_{xx}$ for uniaxial strain ϵ_{xx} along x -direction, 5) Young's modulus $E_y = \sigma_{yy}/\epsilon_{yy}$ and 6) Poisson's ratio $\nu_y = -\epsilon_{xx}/\epsilon_{yy}$ for uniaxial strain ϵ_{yy} along y -direction, 6) spring constant k_s for bond stretching and 7) k_b for bond angle bending 8) - 10) the elastic constants $c_{11} = c_{22}$, $c_{12} = \lambda^*$ and $c_{66} = G = \mu$ (G is the shear modulus, and λ and μ the first and second Lamé's coefficients, respectively). Directions x and y correspond to the arm chair and zig-zag directions, respectively. Ab initio and experimental values are included for comparison. The k_s , k_b , c_{11} , c_{12} and c_{66} values in parenthesis, have been calculated by us, based on the average of the provided E and ν values. [1]: (Lynch and Drickamer (1966)), [2]: (Lee et al. (2008)), [3]: graphite (Bosak et al. (2007)), [4]: graphite (Blakslee et al. (1970)), [5]: AIMPRO (Ivanovskaya et al. (2010)), [6]: Siesta (Fthenakis and Menon (2019)), [7]: Quantum Espresso and QM-CPACK (Shin et al. (2014)), [8]: Quantum Espresso (Fthenakis and Lathiotakis (2015; 2017)), [9]: (Jensen et al. (2015)) [10]: (Lebedeva et al. (2019)) [11]: (Qian et al. (2021)), * 2nd minimum, ** ± 150 , *** ± 20 .

ReaxFF or method	U_{coh} (eV/atom)	a_0 (Å)	E_x/E_y (GPa)	ν_x/ν_y	c_{11} (GPa)	c_{12} (GPa)	c_{66} (GPa)	k_s (eV/Å ²)	k_b (eV/Å ²)
Mattsson	-8.912227	1.48495	1014/1016	0.987/0.978	38752	38241	255	2884	1.54
RDX	-8.681633	1.45003	1051/1048	0.984/0.984	33102	32573	264	2375	1.60
lg	-8.773100	1.44998	1087/1084	0.983/0.984	33698	33151	273	2417	1.66
Budzien	-8.527977	1.44761	1060/1056	0.984/0.986	35407	34874	267	2541	1.61
CHO-2008	-8.479561	1.44385	1331/1334	0.983/0.983	40234	39562	336	2885	2.03
CHON-2010	-8.479561	1.44385	1331/1334	0.983/0.983	40234	39562	336	2885	2.03
ci-CH	-8.423060	1.43777	926/936	0.975/0.976	19006	18534	236	1357	1.43
ci-CH*	-8.411486	1.45497	821/819	0.753/0.746	1869	1400	234	118	1.52
GR-RDX-2021	-7.431757	1.42183	795/797	0.550/0.550	1141	628	257	64.0	1.81
C-2013	-7.434825	1.42159	801/795	0.537/0.540	1124	605	259	62.5	1.84
CHO-2016	-7.404626	1.41991	765/772	0.543/0.554	1099	603	248	61.5	1.75
CHON-2019	-7.404626	1.41991	765/772	0.543/0.554	1099	603	248	61.5	1.75
exper. [1]		1.4210							
exper. [2]			1020**						
exper. [3]			(1092)	(0.125)	1109	139	485	(45.1)	(4.78)
exper. [4]			(1030)	(0.17)	1060***	180***	(440)	(44.8)	(4.1)
DFT/PBE [5]	-7.73	1.429							
DFT/PBE [6]		1.4372	964/964	0.189/0.190	(1000)	(189)	(405)	(43.0)	(3.70)
DFT/PBE [7]	-7.906								
QMC [7]	-7.464(10)								
DFT/PBE [8]			1024/1020	0.177/0.173	1054	185	435	44.8	4.04
DFT/PBE-D2 [9]		(1.424)	1046	0.139	1067	148	459	(43.9)	(4.45)
CHO-2008 [10]		1.4438496	1343	0.987	(51992)	(51316)	(338)	(3735)	(2.04)
CHO-2008 [9]		(1.421)	1235	0.876	5320	4662	311	(360)	(2.05)
C-2013 [10]		1.4215522	789.4	0.537	(1109)	(596)	(257)	(61.6)	(1.82)
C-2013 [9]		(1.421)	751	0.502	(1004)	(504)	(250)	(54.5)	(1.81)
C-2013 [11]			920		650				

inherited by C-2013 and can therefore be used to represent carbon foams, nanoporous carbon or diamond-like systems.

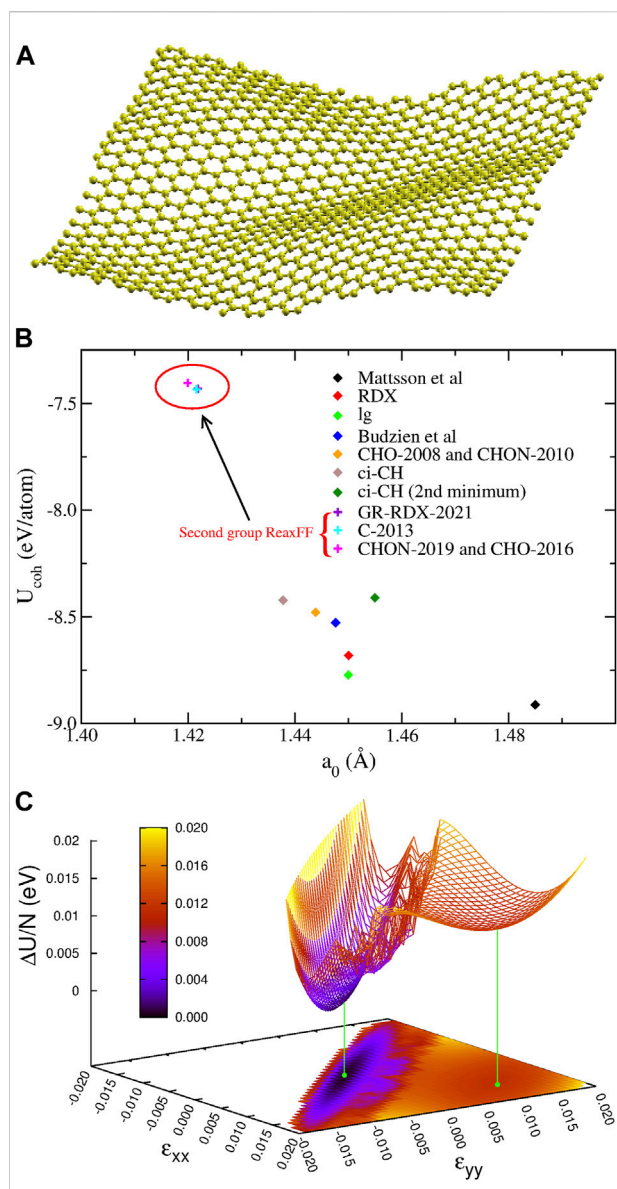
The definition of multiple atom types for carbon brings a disadvantage: if C_g and C atoms interchange their position, the description might be less accurate. However, because C_g -C and C-C interactions are the same, the description is still correct when a C_g atom takes the place of a C atom. Of course the GR-RDX-2021 potential, carries inaccuracies inherent to both RDX and C-2013, as well as possible ones due to the modifications in C-2013 general parameters. The file with the parameters of GR-RDX-2021 in LAMMPS format is included as the Supplementary Information to this work.

3 Results

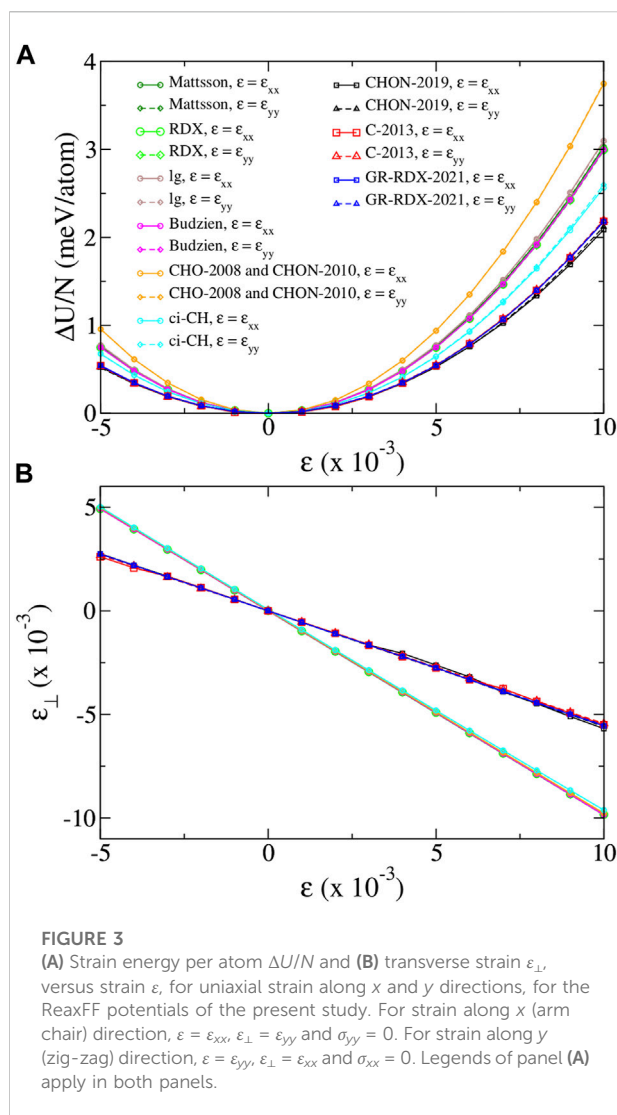
3.1 Graphene

3.1.1 Structural properties and energetics

Here we present our results for the cohesive energy U_{coh} and the structural properties of relaxed graphene structures, obtained with the potentials (1)-(9) and GR-RDX-2021. We started optimizations both by exactly flat and rippled structures, to avoid introducing biases and optimizing both the structure and the supercell size. We found flat exact hexagonal symmetries for the stable state in all cases, though with



different bond lengths, a_0 , reported in Table 1 in descending order, together with the cohesive energies U_{coh} . In the same table, we also report experimental and *ab initio* values for comparison. The potentials can be classified in two groups: the first includes the Mattsson, ci-CH, RDX, lg, Budzien, CHO-2008 and CHON-2010 potentials, and has a_0 in the range $[1.48, 1.44] \text{ \AA}$ and U_{coh} in the range $[-8.9, -8.4] \text{ eV}$; the second includes the GR-RDX-2021, C-2013, CHO-2016 and CHON-



2019 potentials, and a_0 in the range $[1.420, 1.422] \text{ \AA}$ and U_{coh} in the range $[-7.43, -7.40] \text{ eV}$. The values of a_0 for CHO-2008 and C-2013 potentials are in agreement with those found by Lebedeva *et al.* (Lebedeva *et al.* (2019)). The results of U_{coh} versus a_0 are also presented in Figure 2B, where the distinction between the two groups is evident. While the second group reasonably reproduces the experimental values, the first one overestimates a_0 by 1.4–4.2% and U_{coh} (in absolute value) by 13.5–20.3%. The bond length overestimation in first group is not that large, but if the supercell size is forced to a value corresponding to the experimental length of 1.42 \AA , the structure turns to a rippled one, as shown in Figure 2A obtained with CHON-2010. These results, for contracted graphene are in accordance with other DFT results, where similar ripples appear in laterally compressed graphene sheets (Tozzini and Pellegrini (2011); Rossi *et al.* (2015)).

Additionally, ci-CH potential was found to have two minima differing by 0.0116 eV/atom, whose structure differs only by the bond length (of 1.2%), the shorter one being more stable. In order to better understand the origin of this splitting, we calculated the potential energy surface (PES) as a function of the strains ε_{xx} , ε_{yy} along the x and y directions, respectively, shown in **Figure 2C**. The saddle point connecting the two minima appears at $\varepsilon_{xx} = \varepsilon_{yy} = 0.006$, and lies 0.0134 eV/atom above the absolute minimum and 0.0018 eV/atom above the secondary one, which is very shallow. Moreover, the transition region between the minima appears rather noisy, possibly due to reasons described below, in **Section 3.1.3**).

3.1.2 Mechanical properties

We calculate the Young's modulus E , and the Poisson's ratio ν for uniaxial strain along x and y directions and, based on them, the elastic constants c_{11} , c_{12} and c_{66} . **Figure 3A** shows the strain energy per atom $\Delta U/N$ of the fully optimized uniaxially strained graphene for low strain values ($-0.005 \leq \varepsilon \leq 0.01$). Here $\Delta U = U(\varepsilon) - U_0$, with U_0 the energy at zero strain. **Figure 3B** shows the corresponding transverse relaxed strain ε_{\perp} vs. the longitudinal imposed one. For small strain values, the energy and the transverse strain has a quadratic and a linear dependence on strain, respectively, as shown in **Figures 3A,B**. We may then write

$$U(\varepsilon_{xx}) = \kappa_x \varepsilon_{xx}^2 + U_0 \quad (1)$$

$$\varepsilon_{\perp} = \varepsilon_{yy} = -\nu_x \varepsilon_{xx} \quad (2)$$

where ν_x is the Poisson's ratio for strain along x direction. It is easy to show that

$$E_x = \sigma_{xx} / \varepsilon_{xx} = 2\kappa_x / V, \quad V = L_x L_y d_0, \quad (3)$$

with E_x being the Young's modulus for strain along x and V the volume evaluated using the xy supercell size and the sheet thickness $d_0 = 3.34 \text{ \AA}$, corresponding to the graphite interlayer separation distance (**Fthenakis and Lathiotakis (2015)**). The corresponding equations along y direction are obtained by interchanging x with y , i.e., $U(\varepsilon_{yy}) = \kappa_y \varepsilon_{yy}^2 + U_0$, $\varepsilon_{\perp} = \varepsilon_{xx} = -\nu_y \varepsilon_{yy}$, and $E_y = \sigma_{yy} / \varepsilon_{yy} = 2\kappa_y / V$. The values of κ_x and κ_y (and of E_x and E_y) can be found with a quadratic fit of the $(\varepsilon, \Delta U/N)$ points of **Figure 3A**, while ν_x and ν_y with a linear fit to $(\varepsilon, \varepsilon_{\perp})$ of **Figure 3B**. The E_x , E_y , ν_x and ν_y values found here for the ReaxFF potentials are reported in **Table 1**, and compared with the DFT theoretical predictions and experimental values, as well as, with the results found by Qian *et al* (**Qian et al. (2021)**) for C-2013 potential, and by Jensen *et al* (**Jensen et al. (2015)**) and Lebedeva *et al* (**Lebedeva et al. (2019)**) for both C-2013 and CHO-2008 potentials.

We first observe that **Figure 3** shows basically no anisotropy: all curves depending on ε_{xx} superimpose to the corresponding for ε_{yy} , leading to (almost) identical values of the corresponding elastic moduli. **Figure 3B** also clearly shows that

all data collapse on two lines only, corresponding to potentials of the two groups previously defined according to the cohesive energy predictions. The first group returns an unrealistically high $\nu \sim 0.983\text{--}0.987$, while the second returns values $0.537\text{--}0.554$ nearer to the DFT one, although still substantially overestimated. In turn, the curves of panel 1) for the potentials of the first group are very similar, yielding $E \sim 926\text{--}1,087$ GPa, while for the potentials of the second group they collapse to the same curve yielding $E \sim 765\text{--}801$ GPa. The results we find for the CHO-2008 potential, are very similar with those found by Lebedeva *et al* (**Lebedeva et al. (2019)**), although not very similar with those found by Jensen *et al* (**Jensen et al. (2015)**). Moreover, the results we find for the C-2013 potential are very similar with those found by both Lebedeva *et al* (**Lebedeva et al. (2019)**) and Jensen *et al* (**Jensen et al. (2015)**), though slightly different from those of Qian *et al* (**Qian et al. (2021)**). Therefore, on average, E values from first group matches better experimental and DFT data than that by the second, which yields a value lower by at least 25%. This could have been considered as a success of the first-group potentials, if their ν values were not so large, meaning that deformations would be practically achieved only through bond angle bending, with negligible bond stretching.

Table 1 also reports the elastic constants, related to ν and E (see Ref. **Chou and Pagano (1992)**)

$$c_{11} = c_{22} = \frac{E}{1 - \nu^2}, \quad (4)$$

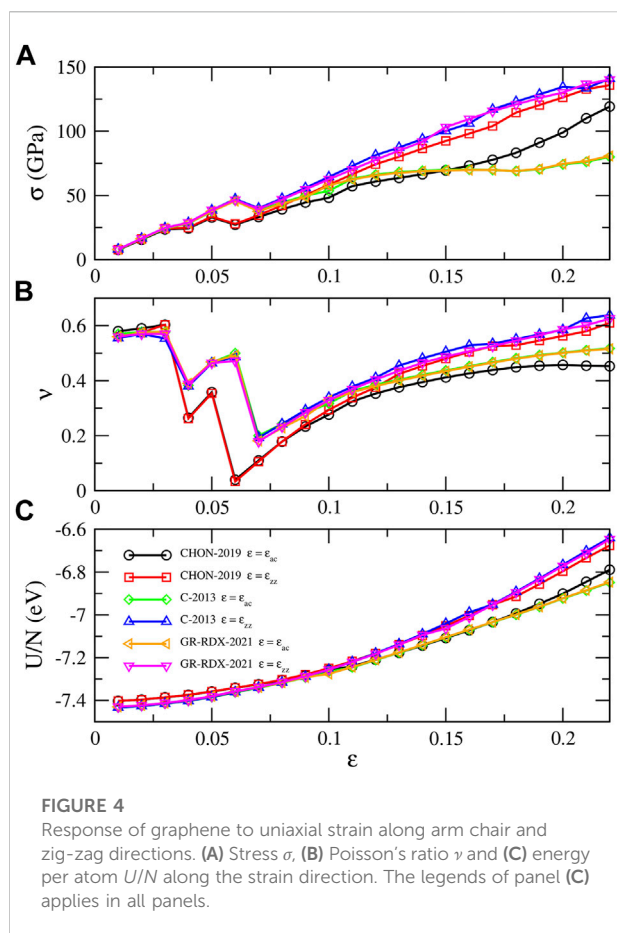
$$c_{12} = \lambda^* = \frac{E\nu}{1 - \nu^2}, \quad (5)$$

$$c_{66} = G = \mu = \frac{E}{2(1 + \nu)}, \quad (6)$$

with these equations being valid for isotropic 2D materials. G is the shear modulus, coinciding with the second Lamé's coefficient μ , and λ^* is the first Lamé's coefficients for 2D isotropic materials (differing by its three-dimensional version which is $\lambda = \nu E / [(1 + \nu)(1 - 2\nu)]$). The elastic constants c_{11} and c_{12} predicted by the potentials of the first group are extremely high due to the $1 - \nu^2$ in the denominator of **Eqs. 4, 5**. For the second group the c_{11} values are very close to those derived from DFT, but the c_{12} are approximately 3–4 times larger. As for the shear modulus G (or the c_{66} elastic constant), the first and second group predict more or less the same value, approximately half the value derived by DFT.

To understand the origin of the discrepancies between the ReaxFF potentials and the experimental and DFT results, we evaluate the bond stretching and bending spring constants k_s and k_b of an equivalent stick and spiral model in terms of E and ν . Within this model (**Fthenakis and Lathiotakis (2017)**) the deformation energy ΔU of graphene is

$$\Delta U = \frac{1}{2} \sum_i \left(k_s \delta l_i^2 + \frac{1}{2} \sum_j k_b a_0^2 \delta \phi_{ij}^2 \right), \quad (7)$$



where $\delta l_i = l_i - a_0$ is i th bond elongation, $\delta\phi_{ij} = \phi_{ij} - \phi_0$ is the deformation of the angle between bonds i and j with respect to the sp^2 angle $\phi_0 = 120^\circ$. Using Eq. 7, one gets

$$E = \frac{8\sqrt{3}}{d_0} \frac{k_s k_b}{k_s + 18k_b} \quad \text{and} \quad \nu = \frac{k_s - 6k_b}{k_s + 18k_b} \quad (8)$$

or equivalently

$$k_s = \sqrt{3}d_0 \frac{E}{1-\nu} \quad \text{and} \quad k_b = \frac{d_0}{2\sqrt{3}} \frac{E}{3\nu+1}. \quad (9)$$

Fitting DFT data (Fthenakis and Lathiotakis (2017)) to this model leads to the values $k_s \approx 45 \text{ eV/\AA}^2$ and $k_b \approx 4 \text{ eV/\AA}^2$, in consistency with $E = 1,012 \text{ GPa}$ and $\nu = 0.1744$ also obtained by DFT (Fthenakis and Lathiotakis (2015)). Using the E and ν values for each potential we derived k_s and k_b , shown in the last columns of Table 1. As previously, the spring constants are different for the two potential groups. For the first group, k_s is 1,357–2,885 eV/\AA^2 and k_b 1.43–2.03 eV/\AA^2 , i.e. the bond stretching is 30–64 times stronger than that provided by DFT, while the bond-angle bending is weaker by a factor $\approx 1/3 - 1/2$. The extremely high k_s values are due to near unit value of ν in the potentials of the first group. For the second group, $k_s \approx 61.5\text{--}64 \text{ eV/\AA}^2$ and $k_b \approx 1.75\text{--}1.84 \text{ eV/\AA}^2$, i.e., only $\approx 4/3$ stronger and $\approx 2/5$ weaker than

the corresponding DFT values, respectively. As a consequence, the energy penalty e.g. for $\epsilon = 0.01$ stretching in the first group, is $\Delta U = 260 \text{ meV}$, while the same amount of energy is sufficient to generate an angular distortion as large as $\delta\phi = 23^\circ$, or a stretching of up to 7% with the potentials of the second group or DFT. Conversely, for the second group, the amount of energy needed for a stretching of 1% is only 4.5–6.3 meV. As a summary of the above discussion, and to highlight the importance of the correct reproduction of the Poisson ratio, we observe that from Eq. 9 one gets

$$\frac{k_s}{k_b} = 6 \frac{3\nu + 1}{1 - \nu}, \quad (10)$$

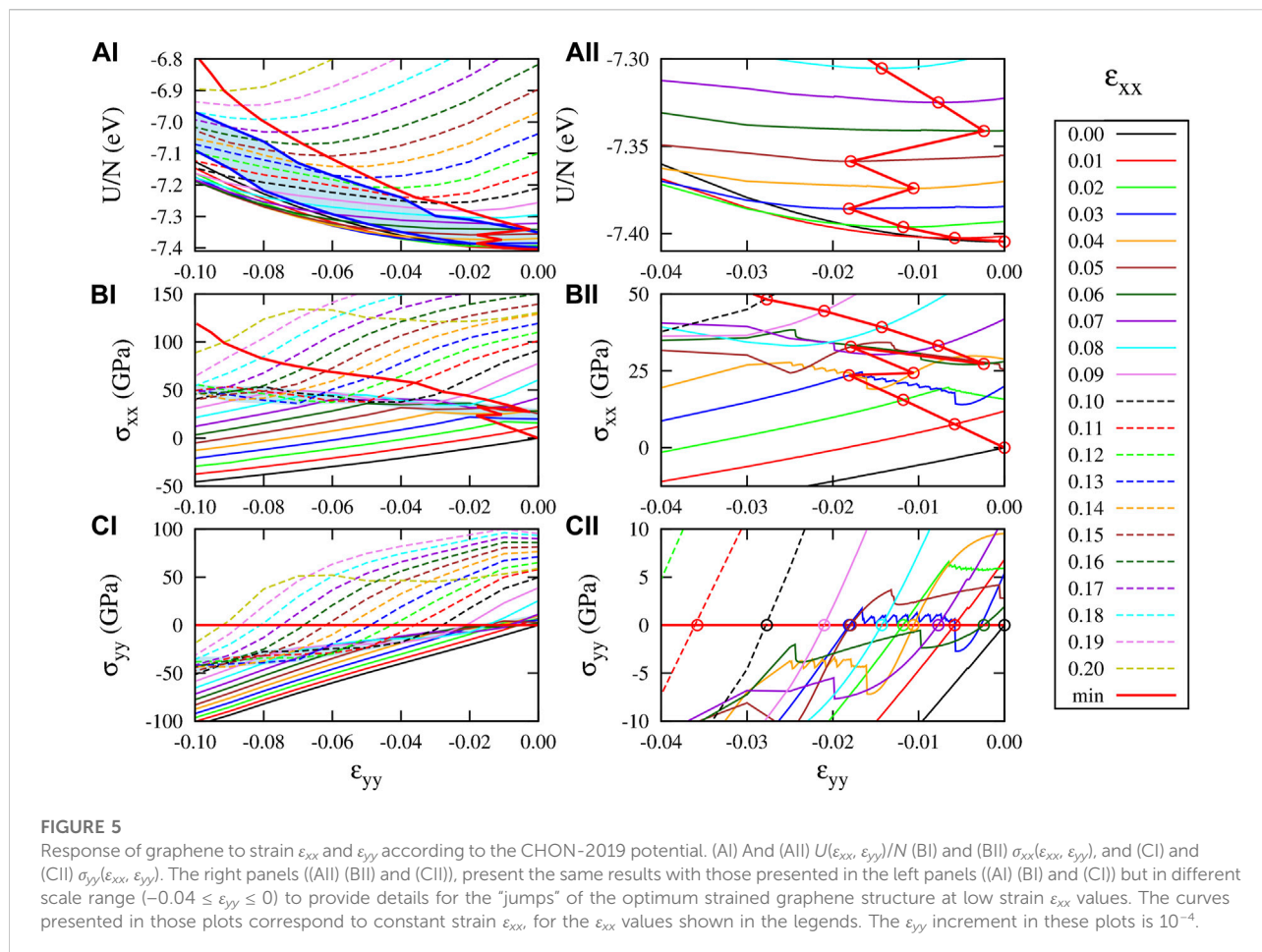
which clearly shows the divergence of the k_s/k_b ratio as $\nu \rightarrow 1$. In conclusion, the potentials of the first group might provide unreliable results for graphene. Therefore, in the following we will focus only on those of the second group.

3.1.3 Response to strain

Figure 4 shows the energy per atom (U/N), stress (σ) and Poisson's ratio (ν) vs. ϵ of the potentials of the second group, for uniaxial strain along zig-zag and arm chair directions in the range $[0, 0.22]$. The results by C-2013 and GR-RDX-2021 are similar, and not very different from those by CHON-2019. The behavior is isotropic at low strain values, while anisotropy appears at $\epsilon \gtrsim 0.10$. The break of isotropy and harmonicity occurs even earlier, at $\epsilon = 0.07$ in panel (a), while DFT calculations (Fthenakis and Menon (2019); Fthenakis and Lathiotakis (2015)) show a similar behavior at $\epsilon \gtrsim 0.15$. ReaxFF agrees with DFT in predicting a smaller stiffness at large stress along the zig-zag with respect to the armchair direction.

Additionally, the stress in Figure 4A shows a net drop occurring at $\epsilon \approx 0.05\text{--}0.06$ for the different potentials, also observed in the studies by Jensen *et al* (Jensen *et al.* (2015)) and by Qian *et al* (Qian *et al.* (2021)). These “drops” are accompanied by strain “jumps” in the lateral direction, which results in corresponding “jumps” in the Poisson's ratio (panel B). Similar results for the Poisson's ratio were obtained by Lebedeva *et al* (Lebedeva *et al.* (2019)) using the C-2013 ReaxFF. While up to $\epsilon \approx 0.03$ the sheet normally “shrinks” in the lateral strain direction at $\epsilon \approx 0.04$ it displays an expansion and a subsequent shrinking, but with different coefficients dependent on the potentials. These drops repeat a couple of time before ν assumes a monotonically increasing though non linear behavior. These alternating jumps in ν are not observed in DFT studies (Fthenakis and Menon (2019); Fthenakis and Lathiotakis (2015)), where a smoothly decreasing behavior is observed.

To get further insight in this anomalous behavior of ν , we performed a finer sampling of the energy and stress values in the $\epsilon_{xx}\text{--}\epsilon_{yy}$ plane, using CHON-2019, reported as a function of ϵ_{yy} at given values of ϵ_{xx} in Figure 5, left side panels. The right side



panels reports a zoom into the anomalous region. The thick red solid line crossing the curves in each panel connects the equilibrium points at given constant ε_{xx} . The anomalous behavior is visible in (panels B) and (C) of Figure 5 as a narrow shaded strip where the curves change slope. In (panels C) the strip connects approximately the points $(\varepsilon_{yy}, \sigma_{xx}) \approx (-0.10, 50 \text{ GPa}) - (0, 25 \text{ GPa})$, in (panels C) the points $(\varepsilon_{yy}, \sigma_{yy}) \approx (-0.10, -40 \text{ GPa}) - (0, 5 \text{ GPa})$. Below the strip, the system behaves elastically, with almost linear dependence of σ on ε . Above the strip, the behavior appears again almost linear, but with a different slope suddenly changing in the strip area. For instance, the stress curve for $\varepsilon_{xx} = 0.09$ change its slope at $\varepsilon_{yy} \approx -0.03$ and $\varepsilon_{yy} \approx -0.08$. The corresponding transition area in the energy plots (panels A) has clearly a curve shape less easily identifiable, which can be estimated from the $\sigma - \varepsilon$ plots. In panel (AI) it is shown as the shaded area between the thick blue lines.

Inside the border strips, the system displays on average an opposite dependence of strain on stress, which can be roughly estimated as the slope of the strip itself, namely $\approx -250 \text{ GPa}$ for σ_{xx} and $\approx 450 \text{ GPa}$ for σ_{yy} . The negative and positive slopes along x and y directions, respectively, show the tendency of the PES

inside that area to form a saddle point. In general, therefore, moving along the red lines in (panels B) and (C), one crosses the different ε_{xx} lines and can rebuilt plots of Figure 4. Thus, for $0 \geq \varepsilon_{xx} \geq 0.03$, the energy minimum falls in the region below that strip, exhibiting a linear-like behavior between stress and strain with a specific slope, as shown in Figure 4A, which is also depicted as a linear relation of ν versus strain in Figure 4B for that strain range. For $0.03 < \varepsilon_{xx} < 0.07$, however, it falls inside that strip area and the slope of σ_{xx} versus ε_{xx} changes having an irregular (not linear) behavior, which is also depicted in the stress-strain plot of Figure 4A for that strain range. Thus, graphene in the lateral strain direction either enlarges or shrinks also irregularly, causing the irregular behavior of ν , which can be seen in Figure 4B for that strain range. For $\varepsilon_{xx} \geq 0.07$ the energy minimum falls in the region above that strip, exhibiting again an almost linear behavior, as shown by the thick red line of Figure 5B and Figure 4A.

Beyond that anomalous behavior of graphene PES, panels (BII) and (CII) of Figure 5 also show some discontinuities in the stress-strain curves. These discontinuities are more pronounced in the stress-strain curves between σ_{xx} and σ_{yy} versus ε_{xx} for

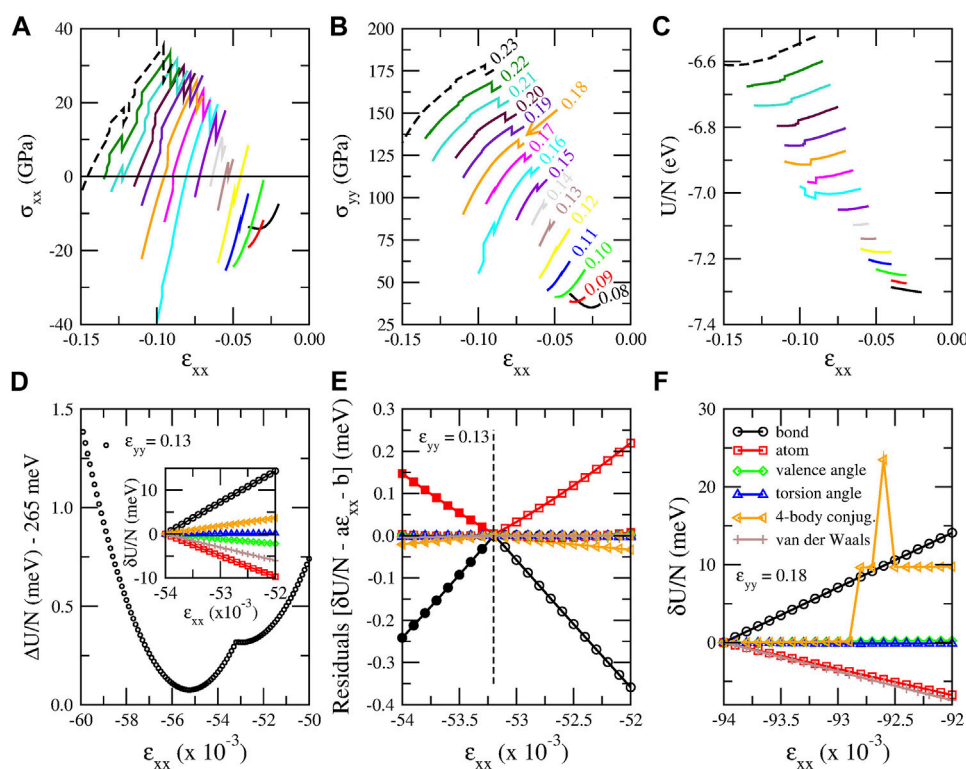


FIGURE 6

(A)–(C) “Jumps” (discontinuities) in stress and energy plots obtained using the CHON-2019 potential. (A) Stress along x direction (σ_{xx}), (B) stress along y direction (σ_{yy}) and (C) energy per atom (U/N) as a function of strain along x direction (ϵ_{xx}) for fixed ϵ_{yy} values indicated with different colors. The ϵ_{yy} value corresponding to each curve of panels (A), (B) and (C) is shown next to each curve in panel (B) with the same color. (D) Strain energy per atom $\Delta U/N = U/N - U_{coh}$, shifted by 265 meV versus ϵ_{xx} for $\epsilon_{yy} = 0.13$, showing the discontinuous change in the energy slope. In the inset: energy per atom for the six terms constituting the energy of the system. Each energy term is shifted by the value it has for $\epsilon_{xx} = -0.0540$. (E) Residuals between the energy per atom values of each energy term shown in the inset of panel (D) and their fitted linear functions for $-0.0540 \leq \epsilon_{xx} \leq -0.0532$ (open symbols) and for $-0.0532 \leq \epsilon_{xx} \leq -0.0520$ (solid symbols). The residuals are calculated for all the energy values in the $[-0.0540, -0.0520]$ interval and not only for the values used for the fitting. (F) The six energy terms for $\epsilon_{yy} = 0.18$ and $-0.0940 \leq \epsilon_{xx} \leq -0.0920$. The legends of panel (F) apply both in panel (E) and the inset of panel (D). The ϵ_{xx} increment in all these plots is 10^{-4} .

constant ϵ_{yy} values, as shown in Figures 6A,B, where different color curves correspond to different ϵ_{yy} values, as shown with the corresponding colored legends in panel (B). These stress discontinuities are caused as an effect of the discontinuity of the first derivative of the energy with respect to ϵ_{xx} , as Figure 6D shows for $\epsilon_{yy} = 0.13$. In particular, for $\epsilon_{yy} = 0.13$ (and strain values close to that), two minima of the energy curve as a function of strain appear, since σ_{xx} becomes zero twice (before and after the discontinuity), as Figure 6A shows. These minima can be also seen in Figure 6D.

The ϵ_{xx} values at which those discontinuities take place perfectly fit to a quadratic function of ϵ_{yy} , as Supplementary Figure S1 shows the interatomic distance distributions for the discontinuity strain values reveals that those discontinuities take place when some second nearest neighbor distances (which for the CHON-2019 potential take the value of 2.459 Å at equilibrium), cross the value of 2.45 Å, as ϵ_{xx} decreases taking negative values for a constant ϵ_{yy} value.

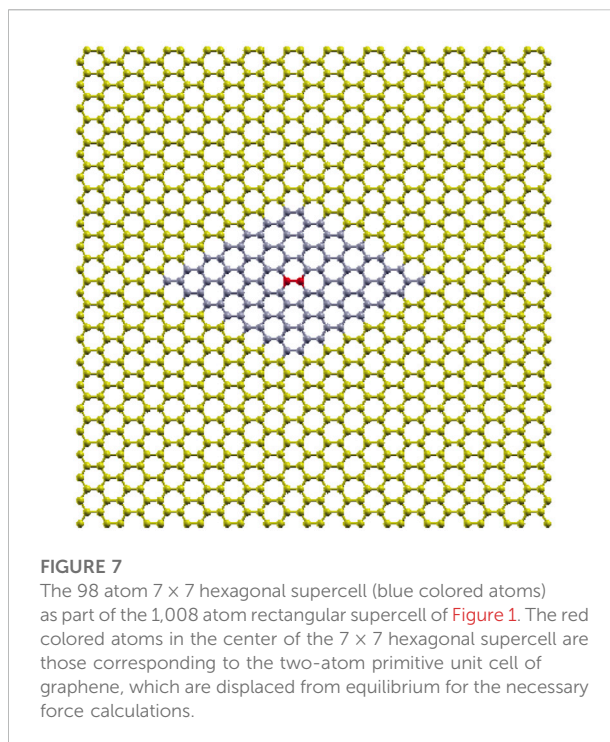
This is a strong indication that these discontinuities are probably due to some cutoff distance, which is used either by LAMMPS implementation of the ReaxFFs or the ReaxFFs themselves to define the bonds, by eliminating the bond order contributions for interatomic distances beyond that cutoff value. This indication is amplified by the fact that the interatomic distance r_{C-C} dependence of the carbon-carbon bond order, which is used in ReaxFFs, practically vanishes for $r_{C-C} > 2.5$ Å (see Ref. van Duin et al. (2001)). Moreover, for the saddle point of the ci-CH potential, which was discussed earlier in section 3.1.1, the distance between second nearest neighbors is 2.505 Å, which is very close to the 2.445 Å distance, which is found here. This indicates that maybe that saddle point and the second minimum, which appear in that case, are of the same origin as the discontinuity of the first derivative of the energy curve and the second energy minimum, respectively, which are shown in Figure 6D.

Interestingly, it appears that not only the stress, but also the energy curves have discontinuities, as **Figure 6C** shows, where the energy per atom versus ϵ_{xx} is plotted for constant ϵ_{yy} values. Those discontinuities appear in different strain ϵ_{xx} values compared with those already described and it is expected that they are also associated with similar cutoff distances and are also shown in **Supplementary Figure S1**. These energy discontinuities should possibly be considered in further improvements.

Similar discontinuities of the stress and the energy were also obtained using the C-2013 and GR-RDX-2021 potentials, as shown in the corresponding **Supplementary Figure S1,S3**.

These observations are in agreement with the findings of Furman and Wales (**Furman and Wales (2019)**), who also studied those discontinuities of ReaxFFs. According to their observations in the dissociation of N_2 , the bond energy term features a cusp at approximately 2.5\AA , causing the first derivative of the bond energy to be discontinuous at this point. Those discontinuities were attributed to several bond order and bond distance cutoffs, in agreement with our suspicions. For the elimination of those discontinuities the authors proposed the use of tapering functions, which would allow a smooth transition between bonded and nonbonding environments. However, such tapering functions or any other way to eliminate those discontinuities are not yet included in the ReaxFFs.

To shed more light in those discontinuities, we examined which energy terms among those composing the CHON-2019 ReaxFF potential are responsible for those discontinuities. In the case of strained graphene six such terms exist, namely the atom, bond, valence angle, torsion angle, 4-body conjugation and van der Waals terms. We examined two cases, 1) one for which the energy is continuous and its first derivative $\partial U/\partial\epsilon_{xx}$ discontinuous, and 2) one for which the energy itself is discontinuous in a ϵ_{xx} range for constant ϵ_{yy} . For the former we selected $\epsilon_{yy} = 0.13$ and $-0.054 \leq \epsilon_{xx} \leq -0.052$, corresponding to the energy curve shown in **Figure 6D**. For this case the discontinuity of $\partial U/\partial\epsilon_{xx}$ occurs at $\epsilon_{xx} = -0.0532$. For the later we selected $\epsilon_{yy} = 0.18$ and $-0.094 \leq \epsilon_{xx} \leq -0.092$, where the energy is discontinuous more than once between $\epsilon_{xx} = -0.0929$ and -0.0925 . For the former the six energy terms are shown in the inset of **Figure 6D**, shifted by the value they have for $\epsilon_{xx} = -0.0540$. Due to the small ϵ_{xx} range, all terms which are not responsible for the $\partial U/\partial\epsilon_{xx}$ discontinuity are expected to be linear functions of ϵ_{xx} . Although the curves shown in the inset of **Figure 6D** give the impression of a linear dependence of those terms on ϵ_{xx} , it is not linear for all terms. This can be seen in **Figure 6E**, which shows the residuals $\delta U/N - a\epsilon_{xx} - b$ between the shifted energy values $\delta U/N$ for each term and the fitting functions $a\epsilon_{xx} + b$ of $\delta U/N$ in the range before and after the discontinuity of $\partial U/\partial\epsilon_{xx}$, i.e. for $-0.0540 \leq \epsilon_{xx} \leq -0.0532$ and for $-0.0532 \leq \epsilon_{xx} \leq -0.0520$, respectively. If the dependence of $\delta U/N$ on ϵ_{xx} is linear, then the two fitting functions should more or less coincide and the residuals, not only in the fitted interval, but also in the extrapolated interval should be practically zero. If, on the other



hand, the residuals in the extrapolated interval is not zero, this means that the slope of the linear fitting function changes, indicating a discontinuous behavior of the derivative $\partial U/\partial\epsilon_{xx}$ of that energy term. As one can see in **Figure 6E**, the slope of the bond and atom energy terms change significantly, with a smaller slope change for the 4-body conjugation term. Consequently, the discontinuity of $\partial U/\partial\epsilon_{xx}$ is caused mainly due to the strain dependence of the bond and atom term of the energy, with a smaller contribution from the 4-body conjugation term. For the later the energy terms are depicted in **Figure 6F**, which shows that the discontinuity in that case clearly comes from the 4-body conjugation term. All other terms are continuous.

It is worth noting that the behavior described above is not associated to anomalous elongation of bonds, or rupture, which have been observed for large positive values of both ϵ_{xx} and ϵ_{yy} . For graphene under strain along x and/or y direction there are only two kind of bonds with different lengths, namely those aligned along x direction, with bond length a , and those belonging to the zig-zag chains along the y direction, with bond length b . Moreover, there are two different types of bond angles, namely the angles ϕ formed between the bonds of those zig-zag chains, and the angles θ formed by the bonds of those zig-zag chains and the bonds directed along the x direction. The angles ϕ and θ depend with each other through the relation $\theta = \pi - \phi/2$. The discontinuities of the derivative $\partial U/\partial\epsilon_{xx}$ (i.e., the sharp change of the slope of the energy, like the one shown in

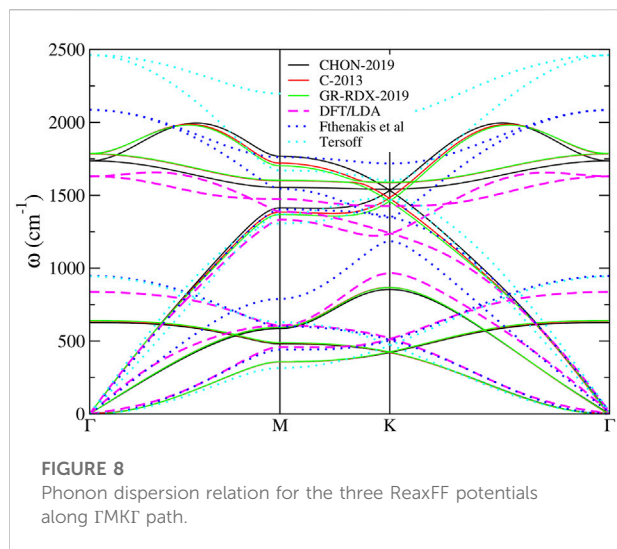


FIGURE 8
Phonon dispersion relation for the three ReaxFF potentials along Γ MK Γ path.

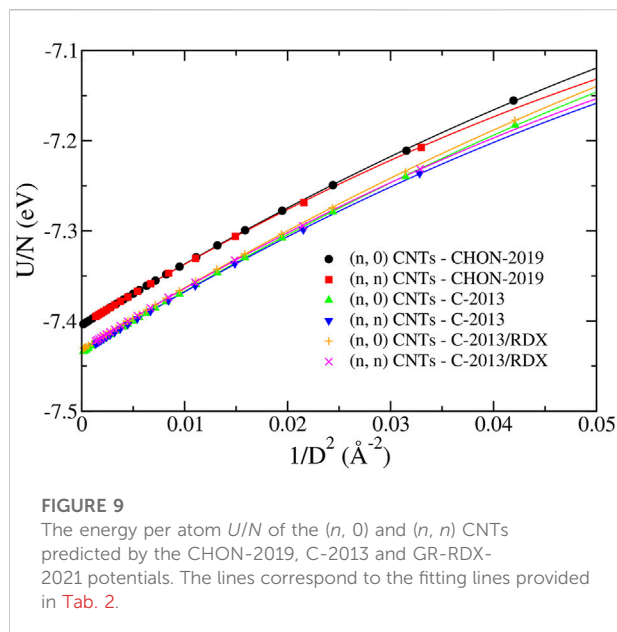


FIGURE 9
The energy per atom U/N of the $(n, 0)$ and (n, n) CNTs predicted by the CHON-2019, C-2013 and GR-RDX-2021 potentials. The lines correspond to the fitting lines provided in Tab. 2.

Figure 6D) do not seem to affect the smooth change of a , b and ϕ as a function of strain ϵ_{xx} . However, the discontinuities of $U(\epsilon_{xx})$ affects a , b and ϕ , which are also discontinuous as a function of ϵ_{yy} . As examples of those cases we show in Supplementary Figure S4 the a , b and ϕ values of the equilibrium structure of graphene under strain $\epsilon_{xx} = 0.13$ (left panels) and 0.18 (right panels) as a function of ϵ_{yy} in a ϵ_{yy} range, where for the former U is continuous and $\partial U/\partial \epsilon_{yy}$ discontinuous, and for the latter U is discontinuous.

3.1.4 Phonon dispersion relation

For the phonon dispersion relation we use an in-house code made by one of us, implementing the frozen phonons method²: The forces on all atoms of a 7×7 portion of the supercell, shown in Figure 7 (blue and red colored), are calculated for $\pm \delta x$, $\pm \delta y$ and $\pm \delta z$ displacements of the atoms of the central unit cell (red colored). For our calculations, we chose $\delta x = \delta y = \delta z = 0.0001 \text{ \AA}$. Those forces are used to calculate numerically the second derivatives of the energy. E.g., for a displacement $\pm \delta y$, one has

$$\frac{\partial^2 U}{\partial x_i \partial y_j} \approx \frac{f_{i,x}(y_j - \delta y) - f_{i,x}(y_j + \delta y)}{2\delta y}, \quad (11)$$

where $f_{i,x}(y_j \pm \delta y)$ denotes the x component of the force \mathbf{f}_i on i th atom. The k dependent dynamical matrix is then evaluated by discrete Fourier transform and diagonalized to get the different branches of dispersion relations.

The optimized 1008-atom rectangular supercell was used for the calculations. A smaller than a 7×7 force summation truncation introduces errors due to missing terms in the

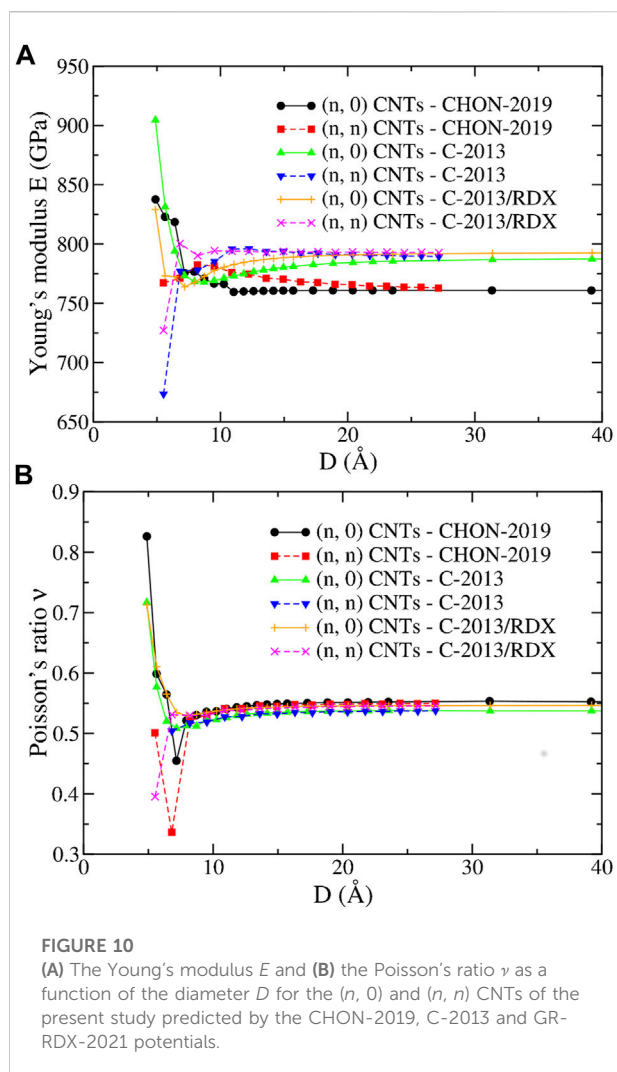
TABLE 2 Fitting functions of the energy per atom U/N of the $(n, 0)$ and (n, n) CNTs for the three ReaxFF potentials. U/N and the CNT diameter D are given in eV and \AA units, respectively.

CNTs	Potential	Equation $U/N =$
$(n, 0)$	CHON-2019	$-7.4043 + 7.0162/D^2 - 26.339/D^4$
$(n, 0)$	C-2013	$-7.4346 + 7.0060/D^2 - 24.683/D^4$
$(n, 0)$	GR-RDX-2021	$-7.4315 + 7.0798/D^2 - 24.900/D^4$
(n, n)	CHON-2019	$-7.4043 + 7.0385/D^2 - 31.710/D^4$
(n, n)	C-2013	$-7.4345 + 6.9853/D^2 - 29.267/D^4$
(n, n)	GR-RDX-2021	$-7.4315 + 7.0732/D^2 - 30.212/D^4$

dynamic matrix, thus producing imaginary frequencies near the Γ point.

The phonon dispersion relations calculated for the potentials of the second group along the Γ MK Γ path in k -space are shown in Figure 8 and compared with 1) DFT results (Fthenakis et al. (2017)), 2) the results of the much simpler molecular mechanics potential of Fthenakis et al. (Fthenakis et al. (2017)) and 3) the Tersoff potential (Tersoff (1988)). As one can see in that figure, the phonon dispersion relations provided by the three potentials are very similar. Quantitative agreement with DFT dispersion relations can also be observed at several parts of the Γ MK Γ path, indicating that these potentials are an improvement with respect to Tersoff and Fthenakis, especially for the representation of the in-plane optical branches. Conversely, the representation of the flexural modes at the zone boundary and of the optical out of plane modes is worse than in Tersoff and Fthenakis.

² The code is available upon request.



3.2 Carbon nanotubes

3.2.1 Energetics

It has been shown that the energy of single-wall carbon nanotubes (CNTs) depends on the diameter D of the CNT, as an effect of the CNT curvature as follows (Tibbetts (1984); Fthenakis et al. (2017); Kanamitsu and Saito (2002)).

$$U/N = U_0 + C_1/D^2 + C_2/D^4 \quad (12)$$

where U_0 is the energy of graphene corresponding to $D = \infty$. The C_1 term is dominant, but C_2 is not negligible. Depending on the method used for the energy calculations, the value of C_1 ranges between ≈ 5 and $\approx 10 \text{ eV}\cdot\text{\AA}^2$ (see Ref. Fthenakis et al. (2017) and references therein).

In Figure 9, we report the energy of the (n, n) and the $(n, 0)$ CNTs as a function of their diameter D , obtained with the three ReaxFF potentials of the second group. The fit with Eq. 12 is reported in Table 2 showing that U_0 differs from the binding

energy of graphene reported in Table 1 by less than 0.004%. The main differences between the curves in Figure 9 are due to this parameter, which differs by 0.03 eV in CHON-2019 potential with respect to others. The parameter $C_1 \approx 7 \text{ eV}\cdot\text{\AA}^2$ for all three potentials and for both $(n, 0)$ and (n, n) CNTs. Moreover, C_2 turns out to be different for $(n, 0)$ and (n, n) CNT's ($\approx -25 \text{ eV}\cdot\text{\AA}^4$ and $\approx -30 \text{ eV}\cdot\text{\AA}^4$, respectively) without significant differences between the three potentials.

3.2.2 Mechanical properties and response to strain

Figure 10 reports E and ν of the $(n, 0)$ and (n, n) CNTs obtained with the ReaxFF potentials of the second group. For $D > 10 \text{ \AA}$, E and ν have a monotonic behavior ultimately leading to the “bulk” graphene values, and independent from the chirality, as expected, and also seen in DFT calculations (Ogata and Shibutani (2003); Qian et al. (2021)). Consequently, as in the “bulk”, E and ν are underestimated and overestimated, respectively, compared DFT calculations. On the other hand, they are coherent with the values obtained with molecular dynamics using C-2013 by Jensen et al (Jensen et al. (2015)) for the (20.0) ($E = 777 \text{ GPa}$) and by Qian et al (Qian et al. (2021)) for the (5.5) ($E = 764 \text{ GPa}$) and for the (10.0) ($E = 825 \text{ GPa}$).

Conversely, the trend for $D \lesssim 10 \text{ \AA}$ is less clear displaying increasing or decreasing behavior and especially opposite divergences at small D depending on the potential, as previously observed (see Ref. Sakharova et al. (2017) and references therein). On the other hand, ν displays a regularly increasing behavior for all three potentials and for both $(n, 0)$ and (n, n) CNTs, for $D \gtrsim 10 \text{ \AA}$, and a minimum at small D whose location and depth is dependent on the potential. However, both the dependence of E and ν on $D > 10 \text{ \AA}$ is rather weak, in accordance with similar studies using other potentials (Fthenakis et al. (2017)).

Panels (A), (B) and (C) of Figure 11 show the energy per atom U/N , the stress σ_{zz} and the Poisson's ratio ν , respectively, of $(n, 0)$ and (n, n) CNTs, calculated using the three ReaxFF potentials, as a function of the strain ϵ_{zz} in the range $[0, 0.5]$. The “drops” shown in Figure 11B at $\epsilon_{zz} \approx 0.05$ are likely to be of the same origin as the corresponding ones discussed for graphene. Accordingly, the plots of ν shown in Figure 11C are very similar with their counterpart for graphene (Figure 4B). There are some differences due to the CNT curvature, mostly affecting CNTs with small diameter. These “drops” for the C-2013 potential can be also seen in the stress - strain plots of the study by Qian et al (Qian et al. (2021)) for the (5.5) and the (10.0) CNTs.

3.2.3 Ultimate tensile strength and fracture strain limits

The energy and stress drops shown in Figures 11A,B at high strain values indicate brittle fractures. The ultimate tensile strength σ_{UTS} (i.e., the maximum stress that can be reached as strain increases)

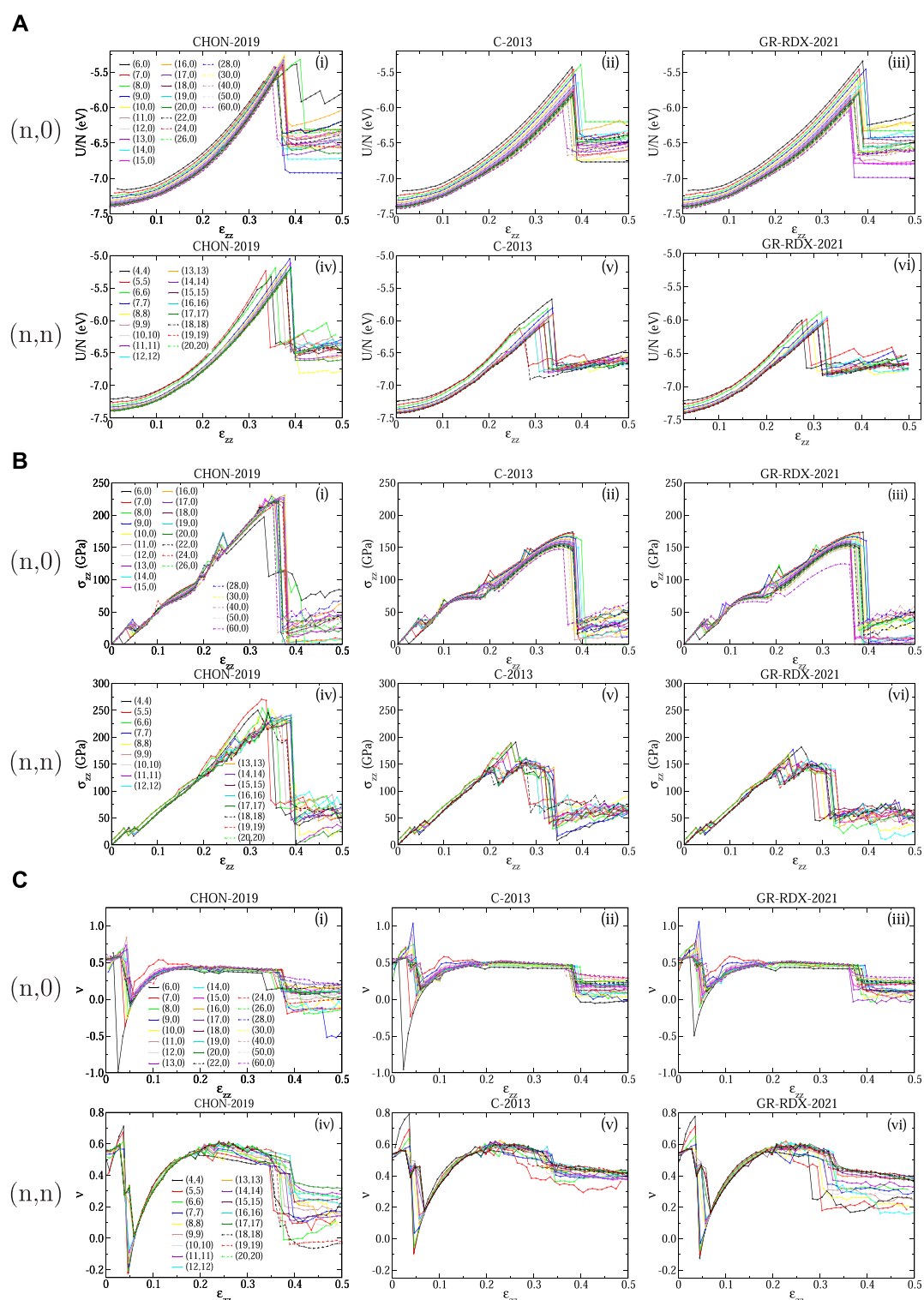


FIGURE 11

Response of CNTs to strain: **(A)** Energy per atom U/N , **(B)** stress σ_{zz} and **(C)** Poisson's ratio ν as a function of strain ϵ_{zz} for $(n, 0)$ (subpanels i, ii, iii) and (n, n) (subpanels iv, v, vi) CNTs predicted using the CHON-2019 (subpanels i, iv), C-2013 (subpanels ii, v) and GR-RDX-2021 (subpanels iii, vi) potential.

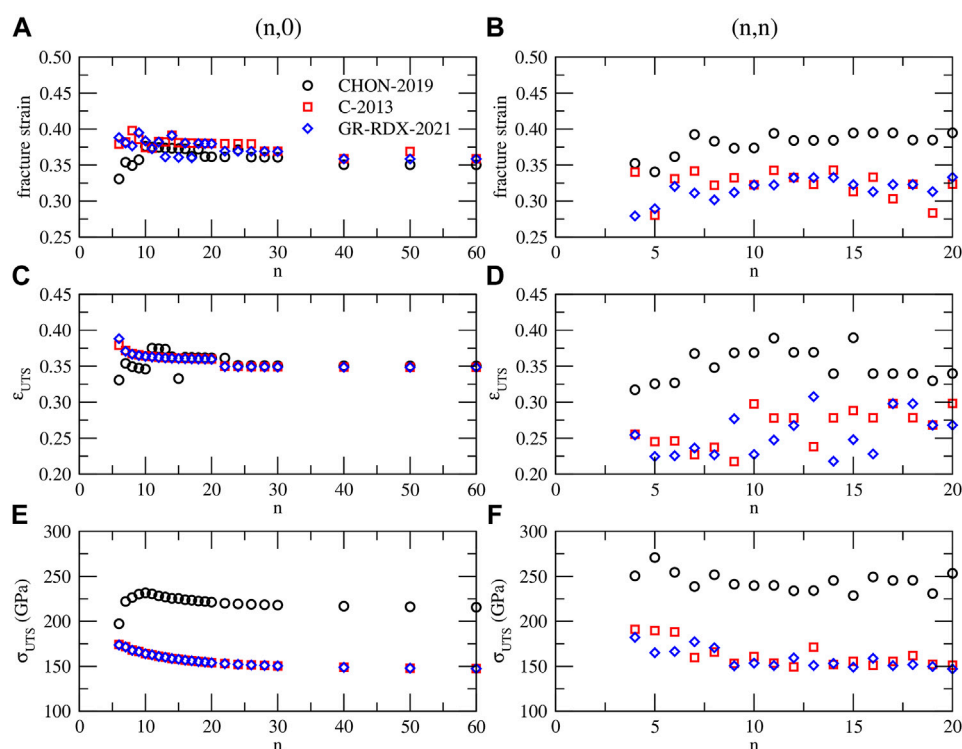


FIGURE 12
(A) and **(B)** fracture strain, **(C)** and **(D)** ultimate tensile strain ϵ_{UTS} , **(E)** and **(F)** ultimate tensile strength σ_{UTS} for $(n, 0)$ (left panels - **(A)**, **(C)** and **(E)**) and (n, n) (right panels - **(B)**, **(D)** and **(F)**) CNTs, predicted by CHON-2019 (black circles), C-2013 (red squares) and GR-RDX-2021 (blue diamonds).

and the corresponding strain ϵ_{UTS} , as well as the fracture strain limits ϵ_F , defined as the strain at which the energy drops occur, are shown in **Figure 12** versus n of the $(n, 0)$ and (n, n) CNTs.

As shown in **Figures 11A,B** the two values ϵ_{UTS} and ϵ_F coincide in many cases, or ϵ_F is slightly larger. For the $(n, 0)$ CNTs they both range between 0.33 and 0.40, with most of the cases ranging between 0.36 and 0.38 for ϵ_F , and 0.35 and 0.37 for ϵ_{UTS} , with not significant differences between the three potentials. For the (n, n) CNTs the ϵ_F and ϵ_{UTS} values are more scattered. Those obtained with CHON-2019 fall in a similar strain range as those for the $(n, 0)$ CNTs, i.e. 0.36–0.39 for ϵ_F and 0.32–0.39 for ϵ_{UTS} , while those from C-2013 and GR-RDX-2021 are smaller for ϵ_F (0.28–0.34) and much smaller for ϵ_{UTS} (0.22–0.31). Concerning σ_{UTS} , values predicted by CHON-2019 both for $(n, 0)$ and (n, n) CNTs are higher than those predicted by C-2013 and GR-RDX-2021, and slightly decreasing with n , although the values for (n, n) CNTs (panel **f**), are more scattered. Moreover, σ_{UTS} from CHON-2019 for $(n, 0)$ CNTs (≈ 230 GPa) are smaller than those for the (n, n) (≈ 250 GPa), while those from C-2013 and GR-RDX-2021 appear almost independent from chirality ($\sigma_{UTS} \approx 160$ GPa). These values of strain fall into the experimental range, which, on average is not larger than $\approx 20\%$, and can be as small as 2%, while σ_{UTS} does not exceed the value of ≈ 150 GPa (Walters et al. (1999); Yu et al.

(2000); Demczyk et al. (2002)), although in some specific experimental conditions much larger values (Bozovic et al. (2003); Troiani et al. (2003)) up to 280% (Huang et al. (2006)) have been reported for ϵ .

On the theoretical side, Ogata and Shibutani (Ogata and Shibutani (2003)) reported a study on (8,0), (9,0), (10,0) and (8,8) CNTs finding $\sigma_{UTS} \sim 86.8\text{--}95.6$ GPa (with tight binding, (TB)) and 117.4–114.6 GPa (with DFT), and $\epsilon_{UTS} \sim 0.170\text{--}0.211$ (with TB) and 0.108–0.110 (with DFT). DFT calculations by Qian et al (Qian et al. (2021)) provide similar results, ≈ 100 GPa for the (10,0), ≈ 92 GPa for the (5,5) CNT, and $\epsilon_{UTS} = 0.22$ for the (5,5) CNT, while for the (10,0) CNT the ϵ_{UTS} was found significantly larger ($\epsilon_{UTS} = 0.33$). Indeed, the values obtained with classical potentials, are found, on average, larger than DFT values. Duan et al (Duan et al. (2007)) reported $\epsilon_{UTS} = 0.2736\text{--}0.4349$ and $\sigma_{UTS} = 99.89\text{--}134.01$ GPa for (10, n) CNTs, $n = 0, 1, 3, 5, 7, 9, 10$, using four classical potentials (COMPASS, a modified Morse, REBO and Dumitrica potentials) while Qian et al (Qian et al. (2021)) found $\sigma_{UTS} = 90\text{--}407.1$ GPa, and $\epsilon_{UTS} 0.19\text{--}0.56$ for (10,0) and (5,5) CNTs, using eight classical potentials (Terstoff and modified Terstoff, AIREBO and modified AIREBO, EDIP, LCBOP, C-2013 and GAP-20). Therefore the results provided by the three ReaxFF potentials of the present study are in line with those of other classical potentials, performing even slightly

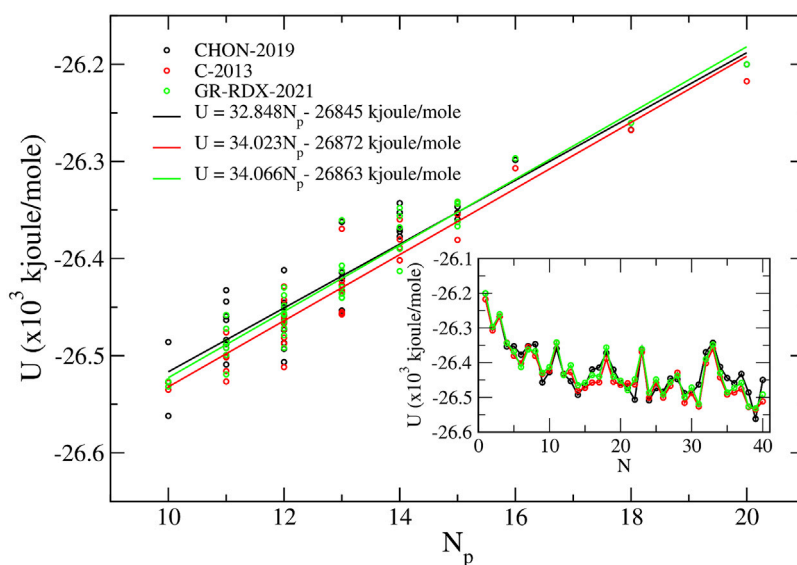


FIGURE 13

Binding energy U of the 40 C_{40} fullerene isomers vs. the pentagon adjacencies N_p calculated using the three ReaxFF potentials. In the inset, we show the calculated energy values versus the standard C_{40} isomer enumeration (Fowler and Manolopoulos (1995)).

better in comparison to DFT. On the other hand, the comparison to experiment is very difficult given the large spread of values.

3.3 Fullerenes and the pentagon adjacency penalty rule

In this part, we calculate the energy U of the icosahedral C_{60} fullerene and the energy of the 40 isomers of C_{40} fullerene, which can be obtained with all possible arrangements of pentagonal and hexagonal rings of the C_{40} fullerene structure (see Refs. Fowler and Manolopoulos (1995), Albertazzi et al. (1999) and Fthenakis et al. (2017)). Albertazzi et al (Albertazzi et al. (1999)) showed that a simple descriptor of the energy of those isomers is the number N_p of pentagon adjacencies and that the energy U of those isomers can be approximated by

$$U = aN_p + b \quad (13)$$

the parameter a ranging between 20 and 100 kJ/mol for different calculations, while for the C_{40} isomers N_p ranges between 10 and 20. Therefore, the maximum energy difference $\Delta U = a\Delta N_p$ of those isomers can be estimated for the maximum values $\Delta N_p = 10$ and $a = 100$ kJ/mol and is of the order of 1,000 kJ/mol (10 eV or 0.25 eV/atom). Similarly, the energy difference between isomers for which the N_p value differs by one can be estimated as 0.025 eV/atom, or even smaller down to 5 meV/atom, which gives an idea of the required sensitivity of the used force field.

At variance with graphene, fullerenes have non-zero torsional angles. In a recent work (Fthenakis et al. (2017)), Fthenakis et al showed the importance of torsional terms in the energy expression of the molecular mechanics potential for sp^2 carbon systems. Neglecting those terms turns out in a poor dependence of the energy of the C_{40} fullerene isomers on N_p , and a strong underestimation of the isomers' energy differences. This may explain the small value of a found by Albertazzi et al with the Tersoff ($a = 24.4$ kJ/mol) and the Brenner ($a = 36.1$ kJ/mol) potentials, which do not explicitly include torsional terms. On the other hand, potentials which include torsional terms, like those by Fthenakis et al (Fthenakis et al. (2017)) or DTMM (Crabbe et al. (1994)) used by Albertazzi et al (Albertazzi et al. (1999)), return higher slope values, although not as high as those given by *ab initio* and semi-empirical methods, which are of the order of 80–100 kJ/mol (see Ref. Albertazzi et al. (1999)).

In Figure 13, we report the energy of the C_{40} isomers as a function of N_p for the three ReaxFF potentials of the second group. The results are compatible with a linear behavior with $a = 32.848$, 34.023 and 34.066 kJ/mol for CHON-2019, C-2013 and GR-RDX-2021, respectively, with correlation coefficient R^2 values of 0.860, 0.918 and 0.922, respectively. These values of a are comparable with those found by the molecular mechanics potentials of Fthenakis et al (Fthenakis et al. (2017)) ($a = 40.5$ kJ/mol) and the DTMM potential (Crabbe et al. (1994)) ($a = 42.2$ kJ/mol), i.e., they are smaller than DFT values, which seems to be a problem, common to all classical potentials, as confirmed by a study (Aghajamali and Karton (2021)) comparing the energy of

the 1812 C_{60} isomers by DFT to those obtained using several potentials including the CHO and the C-2013.

The inset of Figure 13 shows U as a function of standard isomers enumeration, N , used also in Refs. (Fowler and Manolopoulos (1995)), (Albertazzi et al. (1999)) and (Fthenakis et al. (2017)), clearly showing a high correlation among energies predicted by the three ReaxFF potentials of the second group. The optimized C_{40} isomers using the GR-RDX-2021 potential are shown in Supplementary Figure S5. The isomer number ($40:N$) is shown below each structure. It is worth noting that energy differences among the three potentials are less than in graphene. The maximum energy difference per atom in any isomer evaluated with the three potential is of the order of at most 0.016 eV, and 0.003 eV on the average. The corresponding difference for graphene is 0.03 eV/atom (see above).

Among the 12 potentials used in the study by Albertazzi et al (Albertazzi et al. (1999)), all predict isomer no 38 to be the most stable, except Tersoff. Unfortunately, even the three ReaxFF potentials of the second group fail to predict isomer 38 as the most stable. CHON-2019 potential predicts isomer no 39 to be the most stable one, with no 30, 29, 24, 22 and 14 having energies between isomers no 39 and no 38. The energy difference between isomers no 39 and no 38 is 76 kJ/mol, corresponding to 0.78 eV (or 20 meV/atom). C-2013 and GR-RDX-2021 potentials work better in this respect, predicting no 39 to be the most stable one, followed by isomer no 38 with a very small energy difference, 2.0 meV/atom for C-2013 and 1.4 meV/atom for GR-RDX-2021. For completeness, we report that Fthenakis et al (Fthenakis et al. (2017)) find isomer no 38 as the most stable one.

As a final validation check, we evaluated the energy of the icosahedral C_{60} and its difference with respect to graphene using the three potentials of the second group. The values we find with CHON-2019, C-2013 and GR-RDX-2021 potentials, are 0.3625, 0.3759 and 0.3767 eV/atom, respectively, while the corresponding experimental value (Fthenakis (2013); Chen et al. (1991)) is 0.41 ± 0.02 and the one calculated with DFT at the GGA/PBE level (Wirz et al. (2016)) is 0.38 eV/atom. Therefore, the three ReaxFF potentials, although in some cases they fail to capture the very small energy differences between the C_{40} fullerene isomers, they qualitative reproduce the linear increase of the fullerene energy with N_p and correctly predict the relative energy of the icosahedral C_{60} fullerene with respect to graphene.

4 Conclusion

In this work, we study the performance of 11 ReaxFF potentials in reproducing the structural, vibrational and mechanical properties of fullerene, graphene and carbon

nanotubes under strain up to the rupture limit. Ten of them are commonly used general reactive potentials. The 11th one, which we call GR-RDX-2021, is built in this work combining the C-2013 and RDX. The combination is realized defining two different types for carbon atoms belonging to graphene (C_g) or other molecules (C) which are treated with C-2013 and RDX, respectively, to exploit their capabilities to treat graphene and other molecules, respectively, so to optimize the overall performance of the representation. This procedure does not require any further reparameterization and can be easily generalized to any couple of potentials at least in the same class.

According to our findings, seven of these potentials predict unphysical values of the Poisson's ratio describing practically unstretchable graphene bonds in comparison with bond angle deformation. These potentials are not indicated for studies of the elastic properties of sp^2 systems. We focus our study on the four remaining potentials, C-2013, CHO-2016, CHON-2019 and the new one GR-RDX-2021 which do not suffer from such problems. We evaluated the structural and mechanical properties of graphene, its response to tensile stain and its phonon band structure. We studied the energetic and mechanical properties of the $(n, 0)$ and (n, n) CNTs as a function of their diameter, as well as, their response on tensile strain and fracture. We studied the energetics of the 40 C_{40} fullerene isomers and the predictions of the pentagon adjacency penalty rule, as well as, the energy of the icosahedral C_{60} fullerene. The hybrid GR-RDX-2021 potential is tested here on its performances on stretched graphene-derived materials, and is intended to be used to explore the consequences of stretching on the reactivity of graphene with organic molecules including H, O and N, besides C, where it is expected to provide a description at least as good as its parent potential RDX. These aspects are the matter of a forthcoming paper.

Overall, the selected ReaxFF potentials predict practically the same values for graphene bond length (1.42 Å) and cohesive energy (-7.4 eV/atom), in agreement with experimental and DFT values. They also predict similar phonon dispersion relations for graphene, whose discrepancy from DFT is on average similar. Moreover, they all qualitatively and correctly predict: 1) The trend for the energy of CNTs as a function of diameter, 2) the increasing trend of the energy of fullerene isomers as a function of their pentagon adjacencies, and 3) the correct energy difference between the icosahedral C_{60} fullerene with respect to graphene. On the other hand, they underestimate the Young's modulus of both graphene and CNTs by $\approx 3/4$ and overestimate their Poisson's ratio by ≈ 3 times, compared to DFT. In terms of the bond stretching and bond angle bending "spring constants" of an equivalent sticks-spiral mechanical model, the bond stretching is stronger than that provided by DFT by a factor of $\approx 4/3$, while the bond angle bending is weaker by a factor of $\approx 1/2$.

We found unexpected drops and discontinuities in the stress–strain plots, both for graphene and CNT's. We then performed an accurate analysis of the PES as a function of ϵ_{xx} and ϵ_{yy} . Our study revealed several irregularities of the PES (U), including 1) discontinuities of stresses due either to discontinuities of U or its gradients 2) the existence of more than one minimum of U at constant ϵ_{xx} or ϵ_{yy} and 3) changes of the “spring constant” of the equivalent stick–spiral model. Three different regions of the U landscape and corresponding regimes are identified, whose borders crossing is related to the “drops” in the stress–strain plots. Due to those drops, which significantly affect the structural behavior of graphene and CNTs under strain, the dependence of ν on ϵ , for $\epsilon > 0.03$ is rather irregular.

The predictions of the three ReaxFF potentials for the fracture strain, the ultimate tensile strength and the corresponding strain values for the CNTs are overestimated with respect to DFT results. They are, however, in the range of the predictions of other potentials and even closer to the DFT, and fall within the experimental range, which displays a very large variability.

The overall conclusion, therefore, is that the studied ReaxFF potentials, for strain values $\lesssim 0.05$, provide quantitatively reliable results, for the energy and structural properties of graphene, the energetics of CNTs and fullerenes, as well as, the phonon band structure of graphene. Those results are comparable with the corresponding ones of other non-reactive potentials and DFT calculations. On the other hand, further studies are needed at larger stress values. On a qualitative level, reasonable behavior is reproduced displaying the onset of plasticity and rupture, while the quantitative aspects needs further investigations.

The present study, therefore, provides interesting information for the strengths and weakness of those potentials, which hopefully will be useful for their further improvement.

Data availability statement

The original contributions presented in the study are included in the article/**Supplementary Materials**, further inquiries can be directed to the corresponding author.

References

- Abell, G. C. (1985). Empirical chemical pseudopotential theory of molecular and metallic bonding. *Phys. Rev. B* 31, 6184–6196. doi:10.1103/PhysRevB.31.6184
- Aghajamali, A., and Karton, A. (2021). Can force fields developed for carbon nanomaterials describe the isomerization energies of fullerenes? *Chem. Phys. Lett.* 779, 138853. doi:10.1016/j.cplett.2021.138853

Author contributions

ZF performed the calculations, had the idea for the hybrid ReaxFF and wrote the first draft of the paper. VT, NL and IP contributed to the conception and design of the study and to the manuscript revision. All authors read and approved the submitted version.

Funding

This research was funded by the projects (1) EU-H2020 FETPROACT LESGO (Agreement No. 952068), (2) MONSTRE-2D PRIN2017 KFMJ8E of the Italian Ministry of University and Research and (3) “nanoporous GrAphene membrane made without Transfer for gas Separation–GATES” (MIS 5041612), Operational Program “Competitiveness, Entrepreneurship and Innovation” (NSRF 2014–2020) co- financed by Greece and the European Union (European Regional Development Fund).

Conflict of interest

The authors declare that the research was conducted in the absence of any commercial or financial relationships that could be construed as a potential conflict of interest.

Publisher's note

All claims expressed in this article are solely those of the authors and do not necessarily represent those of their affiliated organizations, or those of the publisher, the editors and the reviewers. Any product that may be evaluated in this article, or claim that may be made by its manufacturer, is not guaranteed or endorsed by the publisher.

Supplementary material

The Supplementary Material for this article can be found online at: <https://www.frontiersin.org/articles/10.3389/fchem.2022.951261/full#supplementary-material>

- Albertazzi, E., Domene, C., Fowler, W. P., Heine, T., Seifert, G., Van Alsenoy, C., et al. (1999). Pentagon adjacency as a determinant of fullerene stability. *Phys. Chem. Chem. Phys.* 1, 2913–2918. doi:10.1039/A901600G

- Allinger, N. L., Chen, K., and Lii, J.-H. (1996). An improved force field (mm4) for saturated hydrocarbons. *J. Comput. Chem.* 17, 642–668. doi:10.1002/(SICI)1096-987X(199604)17:5/6<642::AID-JCC6>3.0.CO;2-U

- Allinger, N. L. (1977). Conformational analysis. 130. mm2. a hydrocarbon force field utilizing v1 and v2 torsional terms. *J. Am. Chem. Soc.* 99, 8127–8134. doi:10.1021/ja00467a001
- Allinger, N. L., Yuh, Y. H., and Lii, J. H. (1989). Molecular mechanics. the mm3 force field for hydrocarbons. 1. *J. Am. Chem. Soc.* 111, 8551–8566. doi:10.1021/ja00205a001
- Ashraf, C., and van Duin, A. C. (2017). Extension of the reaxff combustion force field toward syngas combustion and initial oxidation kinetics. *J. Phys. Chem. A* 121, 1051–1068. doi:10.1021/acs.jpca.6b12429
- Beardmore, K., and Smith, R. (1996). Empirical potentials for c[sbnd]si[sbnd]h systems with application to c60 interactions with si crystal surfaces. *Philos. Mag. A* 74, 1439–1466. doi:10.1080/01418619608240734
- Bellucci, L., and Tozzini, V. (2020). Engineering 3d graphene-based materials: State of the art and perspectives. *Molecules* 25, 339. doi:10.3390/molecules25020339
- Berber, S., Kwon, Y.-K., and Tomanek, D. (2000). Unusually high thermal conductivity of carbon nanotubes. *Phys. Rev. Lett.* 84, 4613–4616. doi:10.1103/PhysRevLett.84.4613
- Blakslée, O. L., Proctor, D. G., Seldin, E. J., Spence, G. B., and Weng, T. (1970). Elastic constants of compression-annealed pyrolytic graphite. *J. Appl. Phys.* 41, 3373–3382. doi:10.1063/1.1659428
- Bosak, A., Krisch, M., Mohr, M., Maultzsch, J., and Thomsen, C. (2007). Elasticity of single-crystalline graphite: Inelastic x-ray scattering study. *Phys. Rev. B* 75, 153408. doi:10.1103/PhysRevB.75.153408
- Bozovic, D., Bockrath, M., Hafner, J. H., Lieber, C. M., Park, H., and Tinkham, M. (2003). Plastic deformations in mechanically strained single-walled carbon nanotubes. *Phys. Rev. B* 67, 033407. doi:10.1103/PhysRevB.67.033407
- Brenner, D. W. (1990). Empirical potential for hydrocarbons for use in simulating the chemical vapor deposition of diamond films. *Phys. Rev. B* 42, 9458–9471. doi:10.1103/PhysRevB.42.9458
- Brenner, D. W., Shenderova, O. A., Harrison, J. A., Stuart, S. J., Ni, B., and Sinnott, S. B. (2002). A second-generation reactive empirical bond order (REBO) potential energy expression for hydrocarbons. *J. Phys. Condens. Matter* 14, 783–802. doi:10.1088/0953-8984/14/4/312
- Brooks, B. R., Brucoleri, R. E., Olafson, B. D., States, D. J., Swaminathan, S., and Karplus, M. (1983). Charmm: A program for macromolecular energy, minimization, and dynamics calculations. *J. Comput. Chem.* 4, 187–217. doi:10.1002/jcc.540040211
- Budzien, J., Thompson, A. P., and Zybin, S. V. (2009). Reactive molecular dynamics simulations of shock through a single crystal of pentaerythritol tetranitrate. *J. Phys. Chem. B* 113, 13142–13151. doi:10.1021/jp9016695
- Castro Neto, A. H., Guinea, F., Peres, N. M. R., Novoselov, K. S., and Geim, A. K. (2009). The electronic properties of graphene. *Rev. Mod. Phys.* 81, 109–162. doi:10.1103/RevModPhys.81.109
- Chatzidakis, G. D., Kalosakas, G., Fthenakis, Z. G., and Lathiotakis, N. N. (2018). A torsional potential for graphene derived from fitting to dft results. *Eur. Phys. J. B* 91, 11. doi:10.1140/epjb/e2017-80444-5
- Chelikowsky, J. R. (1992). Formation of c₆₀ clusters via Langevin molecular dynamics. *Phys. Rev. B* 45, 12062–12070. doi:10.1103/PhysRevB.45.12062
- Chen, H. S., Kortan, A. R., Haddon, R. C., Kaplan, M. L., Chen, C. H., Mujsce, A. M., et al. (1991). Reactivity of c₆₀ in pure oxygen. *Appl. Phys. Lett.* 59, 2956–2958. doi:10.1063/1.105810
- Chenoweth, K., van Duin, A. C. T., and Goddard, W. A. (2008). Reaxff reactive force field for molecular dynamics simulations of hydrocarbon oxidation. *J. Phys. Chem. A* 112, 1040–1053. doi:10.1021/jp709896w
- Chou, P. C., and Pagano, N. J. (1992). *Elasticity: Tensor, dyadic and engineering approaches*. New York: Dover.
- Côté, M., Grossman, J. C., Cohen, M. L., and Louie, S. G. (1998). Theoretical study of a three-dimensional all-sp² structure. *Phys. Rev. B* 58, 664–668. doi:10.1103/PhysRevB.58.664
- [Dataset] Crabbe, M. J. C., Appleyard, J. R., and Rees Lay, C. (1994). *Dtmm3.0: Desk-top molecular modeller*.
- Crespi, V. H., Benedict, L. X., Cohen, M. L., and Louie, S. G. (1996). Prediction of a pure-carbon planar covalent metal. *Phys. Rev. B* 53, R13303–R13305. doi:10.1103/PhysRevB.53.R13303
- Demczyk, B., Wang, Y., Cumings, J., Hetman, M., Han, W., Zettl, A., et al. (2002). Direct mechanical measurement of the tensile strength and elastic modulus of multiwalled carbon nanotubes. *Mater. Sci. Eng. A* 334, 173–178. doi:10.1016/S0921-5093(01)01807-X
- Duan, W., Wang, Q., Liew, K., and He, X. (2007). Molecular mechanics modeling of carbon nanotube fracture. *Carbon* 45, 1769–1776. doi:10.1016/j.carbon.2007.05.009
- Dyson, A., and Smith, P. (1996). Extension of the brenner empirical interatomic potential to c-si-h systems. *Surf. Sci.* 355, 140–150. doi:10.1016/0039-6028(96)00004-0
- Elstner, M., Porezag, D., Jungnickel, G., Elsner, J., Haugk, M., Frauenheim, T., et al. (1998). Self-consistent-charge density-functional tight-binding method for simulations of complex materials properties. *Phys. Rev. B* 58, 7260–7268. doi:10.1103/PhysRevB.58.7260
- Fonseca, A. F., Lee, G., Borders, T. L., Zhang, H., Kemper, T. W., Shan, T.-R., et al. (2011). Reparameterization of the rebo-cho potential for graphene oxide molecular dynamics simulations. *Phys. Rev. B* 84, 075460. doi:10.1103/PhysRevB.84.075460
- Fowler, P. W., and Manolopoulos, D. E. (1995). *An atlas of fullerenes*. Oxford: Clarendon Press.
- Fthenakis, Z., Andriotis, A. N., and Menon, M. (2003). Temperature evolution of structural and magnetic properties of transition metal clusters. *J. Chem. Phys.* 119, 10911–10916. doi:10.1063/1.1619931
- Fthenakis, Z. G. (2016). *Ab initio* investigation on the stability of h-6 carbon. *RSC Adv.* 6, 78187–78193. doi:10.1039/C6RA10809A
- Fthenakis, Z. G. (2017). Are the experimentally observed 3-dimensional carbon honeycombs all-sp² structures? The dangling p-orbital instability. *RSC Adv.* 7, 9790–9794. doi:10.1039/C6RA27833G
- Fthenakis, Z. G. (2013). Energetics of graphene flakes. *Mol. Phys.* 111, 3289–3296. doi:10.1080/00268976.2013.782437
- Fthenakis, Z. G., Kalosakas, G., Chatzidakis, G. D., Galiotis, C., Papagelis, K., and Lathiotakis, N. N. (2017). Atomistic potential for graphene and other sp² carbon systems. *Phys. Chem. Chem. Phys.* 19, 30925–30932. doi:10.1039/C7CP06362H
- Fthenakis, Z. G., and Lathiotakis, N. N. (2015). Graphene allotropes under extreme uniaxial strain: An *ab initio* theoretical study. *Phys. Chem. Chem. Phys.* 17, 16418–16427. doi:10.1039/C5CP02412A
- Fthenakis, Z. G., and Lathiotakis, N. N. (2017). Structural deformations of two-dimensional planar structures under uniaxial strain: The case of graphene. *J. Phys. Condens. Matter* 29, 175401. doi:10.1088/1361-648x/aa63d5
- Fthenakis, Z. G., and Menon, M. (2019). Structural deformations and mechanical properties of si₂BN under uniaxial and uniform biaxial strain in comparison with graphene: An *ab initio* study. *Phys. Rev. B* 99, 205302. doi:10.1103/PhysRevB.99.205302
- Fthenakis, Z. G., and Tománek, D. (2012). Computational study of the thermal conductivity in defective carbon nanostructures. *Phys. Rev. B* 86, 125418. doi:10.1103/PhysRevB.86.125418
- Fthenakis, Z. G., Zhu, Z., and Tománek, D. (2014). Effect of structural defects on the thermal conductivity of graphene: From point to line defects to haeckelites. *Phys. Rev. B* 89, 125421. doi:10.1103/PhysRevB.89.125421
- Furman, D., and Wales, D. J. (2019). Transforming the accuracy and numerical stability of reaxff reactive force fields. *J. Phys. Chem. Lett.* 10, 7215–7223. doi:10.1021/acs.jpclett.9b02810
- Hoffmann, R. (1963). An extended hückel theory. i. hydrocarbons. *J. Chem. Phys.* 39, 1397–1412. doi:10.1063/1.1734456
- Huang, J. Y., Chen, S., Wang, Z. Q., Kempa, K., Wang, Y. M., Jo, S. H., et al. (2006). Superplastic carbon nanotubes. *Nature* 439, 281. doi:10.1038/439281a
- Iijima, S. (1991). Helical microtubules of graphitic carbon. *Nature* 354, 56–58. doi:10.1038/354056a0
- Inagaki, M., Qiu, J., and Guo, Q. (2015). Carbon foam: Preparation and application. *Carbon* 87, 128–152. doi:10.1016/j.carbon.2015.02.021
- Ivanovskaya, V. V., Zobelli, A., Teillet-Billy, D., Rougeau, N., Sidis, V., and Briddon, P. R. (2010). Hydrogen adsorption on graphene: A first principles study. *Eur. Phys. J. B* 76, 481–486. doi:10.1140/epjb/e2010-00238-7
- Jang, I., and Sinnott, S. B. (2004). Molecular dynamics simulations of the chemical modification of polystyrene through C_xF_y⁺ beam deposition. *J. Phys. Chem. B* 108, 18993–19001. doi:10.1021/jp049283y
- Jensen, B. D., Wise, K. E., and Odegard, G. M. (2015). Simulation of the elastic and ultimate tensile properties of diamond, graphene, carbon nanotubes, and amorphous carbon using a revised reaxff parametrization. *J. Phys. Chem. A* 119, 9710–9721. doi:10.1021/acs.jpca.5b05889
- Kalosakas, G., Lathiotakis, N. N., Galiotis, C., and Papagelis, K. (2013). In-plane force fields and elastic properties of graphene. *J. Appl. Phys.* 113, 134307. doi:10.1063/1.4798384
- Kalosakas, G., Lathiotakis, N. N., and Papagelis, K. (2021). Width dependent elastic properties of graphene nanoribbons. *Materials* 14, 5042. doi:10.3390/ma14175042

- Kamat, A. M., van Duin, A. C. T., and Yakovlev, A. (2010). Molecular dynamics simulations of laser-induced incandescence of soot using an extended reaxff reactive force field. *J. Phys. Chem. A* 114, 12561–12572. doi:10.1021/jp1080302
- Kanamitsu, K., and Saito, S. (2002). Geometries, electronic properties, and energetics of isolated single walled carbon nanotubes. *J. Phys. Soc. Jpn.* 71, 483–486. doi:10.1143/JPSJ.71.483
- Kański, M., Maciżek, D., Postawa, Z., Ashraf, C. M., van Duin, A. C. T., and Garrison, B. J. (2018). Development of a charge-implicit reaxff potential for hydrocarbon systems. *J. Phys. Chem. Lett.* 9, 359–363. doi:10.1021/acs.jpclett.7b03155
- Khor, K. E., and Das Sarma, S. (1988). Proposed universal interatomic potential for elemental tetrahedrally bonded semiconductors. *Phys. Rev. B* 38, 3318–3322. doi:10.1103/PhysRevB.38.3318
- Kowalik, M., Ashraf, C., Damirchi, B., Akbarian, D., Rajabpour, S., and van Duin, A. C. T. (2019). Atomistic scale analysis of the carbonization process for *c/h/o/n*-based polymers with the reaxff reactive force field. *J. Phys. Chem. B* 123, 5357–5367. doi:10.1021/acs.jpcc.9b04298
- Krainyukova, N. V., and Zubarev, E. N. (2016). Carbon honeycomb high capacity storage for gaseous and liquid species. *Phys. Rev. Lett.* 116, 055501. doi:10.1103/PhysRevLett.116.055501
- Kroto, H. W., Heath, J. R., O'Brien, S. C., Curl, R. F., and Smalley, R. E. (1985). C₆₀: Buckminsterfullerene. *Nature* 318, 162–163. doi:10.1038/318162a0
- Lathiotakis, N. N., Andriotis, A. N., Menon, M., and Connolly, J. (1996). Tight binding molecular dynamics study of ni clusters. *J. Chem. Phys.* 104, 992–1003. doi:10.1063/1.470823
- Lebedeva, I. V., Minkin, A. S., Popov, A. M., and Knizhnik, A. A. (2019). Elastic constants of graphene: Comparison of empirical potentials and dft calculations. *Phys. E Low-dimensional Syst. Nanostructures* 108, 326–338. doi:10.1016/j.physe.2018.11.025
- Lee, C., Wei, X., Kysar, J. W., and Hone, J. (2008). Measurement of the elastic properties and intrinsic strength of monolayer graphene. *Science* 321, 385–388. doi:10.1126/science.1157996
- Lindsay, L., and Broido, D. A. (2010). Optimized Tersoff and Brenner empirical potential parameters for lattice dynamics and phonon thermal transport in carbon nanotubes and graphene. *Phys. Rev. B* 81, 205441. doi:10.1103/PhysRevB.81.205441
- Liu, A. Y., and Cohen, M. L. (1992). Theoretical study of a hypothetical metallic phase of carbon. *Phys. Rev. B* 45, 4579–4581. doi:10.1103/PhysRevB.45.4579
- Liu, H., Wu, S., Tian, N., Yan, F., You, C., and Yang, Y. (2020). Carbon foams: 3d porous carbon materials holding immense potential. *J. Mat. Chem. A* 8, 23699–23723. doi:10.1039/D0TA08749A
- Liu, L., Liu, Y., Zybin, S. V., Sun, H., and Goddard, W. A. (2011). Reaxff-ig: Correction of the reaxff reactive force field for London dispersion, with applications to the equations of state for energetic materials. *J. Phys. Chem. A* 115, 11016–11022. doi:10.1021/jp201599t
- Liu, Y., Wang, G., Huang, Q., Guo, L., and Chen, X. (2012). Structural and electronic properties of *t* graphene: A two-dimensional carbon allotrope with tetrarings. *Phys. Rev. Lett.* 108, 225505. doi:10.1103/PhysRevLett.108.225505
- Los, J. H., and Fasolino, A. (2003). Intrinsic long-range bond-order potential for carbon: Performance in Monte Carlo simulations of graphitization. *Phys. Rev. B* 68, 024107. doi:10.1103/PhysRevB.68.024107
- Los, J. H., Ghiringhelli, L. M., Meijer, E. J., and Fasolino, A. (2005). Improved long-range reactive bond-order potential for carbon. i. construction. *Phys. Rev. B* 72, 214102. doi:10.1103/PhysRevB.72.214102
- Lynch, R. W., and Drickamer, H. G. (1966). Effect of high pressure on the lattice parameters of diamond, graphite, and hexagonal boron nitride. *J. Chem. Phys.* 44, 181–184. doi:10.1063/1.1726442
- Mattsson, T. R., Lane, J. M. D., Cochrane, K. R., Desjarlais, M. P., Thompson, A. P., Pierce, F., et al. (2010). First-principles and classical molecular dynamics simulation of shocked polymers. *Phys. Rev. B* 81, 054103. doi:10.1103/PhysRevB.81.054103
- Mayo, S. L., Olafson, B. D., and Goddard, W. A. (1990). Dreiding: A generic force field for molecular simulations. *J. Phys. Chem.* 94, 8897–8909. doi:10.1021/j100389a010
- Ng, T. Y., Yeo, J., and Liu, Z. (2013). Molecular dynamics simulation of the thermal conductivity of shorts strips of graphene and silicene: A comparative study. *Int. J. Mech. Mat. Des.* 9, 105–114. doi:10.1007/s10999-013-9215-0
- Ni, B., Lee, K.-H., and Sinnott, S. B. (2004). A reactive empirical bond order (REBO) potential for hydrocarbon-oxygen interactions. *J. Phys. Condens. Matter* 16, 7261–7275. doi:10.1088/0953-8984/16/41/008
- Nilsson, L., and Karplus, M. (1986). Empirical energy functions for energy minimization and dynamics of nucleic acids. *J. Comput. Chem.* 7, 591–616. doi:10.1002/jcc.540070502
- Novoselov, K. S., Geim, A. K., Morozov, S. V., Jiang, D., Zhang, Y., Dubonos, S. V., et al. (2004). Electric field effect in atomically thin carbon films. *Science* 306, 666–669. doi:10.1126/science.1102896
- O'Connor, T. C., Andzelm, J., and Robbins, M. O. (2015). Airebo-m: A reactive model for hydrocarbons at extreme pressures. *J. Chem. Phys.* 142, 024903. doi:10.1063/1.4905549
- Ogata, S., and Shibutani, Y. (2003). Ideal tensile strength and band gap of single-walled carbon nanotubes. *Phys. Rev. B* 68, 165409. doi:10.1103/PhysRevB.68.165409
- Pastewka, L., Pou, P., Pérez, R., Gumbsch, P., and Moseler, M. (2008). Describing bond-breaking processes by reactive potentials: Importance of an environment-dependent interaction range. *Phys. Rev. B* 78, 161402. doi:10.1103/PhysRevB.78.161402
- Qian, C., McLean, B., Hedman, D., and Ding, F. (2021). A comprehensive assessment of empirical potentials for carbon materials. *Appl. Mater.* 9, 061102. doi:10.1063/5.0052870
- Rajasekaran, G., Kumar, R., and Parashar, A. (2016). Tersoff potential with improved accuracy for simulating graphene in molecular dynamics environment. *Mat. Res. Express* 3, 035011. doi:10.1088/2053-1591/3/3/035011
- Rappe, A. K., Casewit, C. J., Colwell, K. S., Goddard, W. A., and Skiff, W. M. (1992). Uff, a full periodic table force field for molecular mechanics and molecular dynamics simulations. *J. Am. Chem. Soc.* 114, 10024–10035. doi:10.1021/ja00051a040
- Rossi, A., Piccinin, S., Pellegrini, V., de Gironcoli, S., and Tozzini, V. (2015). Nano-scale corrugations in graphene: A density functional theory study of structure, electronic properties and hydrogenation. *J. Phys. Chem. C* 119, 7900–7910. doi:10.1021/jp511409b
- Sakharova, N. A., Antunes, J. M., Pereira, A. F. G., and Fernandes, J. V. (2017). Developments in the evaluation of elastic properties of carbon nanotubes and their heterojunctions by numerical simulation. *AIMS Mat. Sci.* 4, 706–737. doi:10.3934/mat.2017.3.706
- Schuler, L. D., Daura, X., and van Gunsteren, W. F. (2001). An improved gromos96 force field for aliphatic hydrocarbons in the condensed phase. *J. Comput. Chem.* 22, 1205–1218. doi:10.1002/jcc.1078
- Sheng, X.-L., Cui, H.-J., Ye, F., Yan, Q.-B., Zheng, Q.-R., and Su, G. (2012). Octagraphene as a versatile carbon atomic sheet for novel nanotubes, unconventional fullerenes, and hydrogen storage. *J. Appl. Phys.* 112, 074315. doi:10.1063/1.4757410
- Shi, L., Ma, X., Li, M., Zhong, Y., Yang, L., Yin, W., et al. (2021). Molecular dynamics simulation of phonon thermal transport in nanotwinned diamond with a new optimized Tersoff potential. *Phys. Chem. Chem. Phys.* 23, 8336–8343. doi:10.1039/D1CP00399B
- Shin, H., Kang, S., Koo, J., Lee, H., Kim, J., and Kwon, Y. (2014). Cohesion energetics of carbon allotropes: Quantum Monte Carlo study. *J. Chem. Phys.* 140, 114702. doi:10.1063/1.4867544
- Srinivasan, S. G., van Duin, A. C. T., and Ganesh, P. (2015). Development of a reaxff potential for carbon condensed phases and its application to the thermal fragmentation of a large fullerene. *J. Phys. Chem. A* 119, 571–580. doi:10.1021/jp510274e
- Strachan, A., van Duin, A. C. T., Chakraborty, D., Dasgupta, S., and Goddard, W. A. (2003). Shock waves in high-energy materials: The initial chemical events in nitramine rdx. *Phys. Rev. Lett.* 91, 098301. doi:10.1103/PhysRevLett.91.098301
- Stuart, S. J., Tutein, A. B., and Harrison, J. A. (2000). A reactive potential for hydrocarbons with intermolecular interactions. *J. Chem. Phys.* 112, 6472–6486. doi:10.1063/1.481208
- Sun, H. (1998). Compass: An *ab initio* force-field optimized for condensed-phase applications overview with details on alkane and benzene compounds. *J. Phys. Chem. B* 102, 7338–7364. doi:10.1021/jp980939v
- Takai, T., Lee, C., Halicioglu, T., and Tiller, W. A. (1990). A model potential function for carbon systems: Clusters. *J. Phys. Chem.* 94, 4480–4482. doi:10.1021/j100374a025
- Terrones, H., Terrones, M., Hernández, E., Grobert, N., Charlier, J.-C., and Ajayan, P. M. (2000). New metallic allotropes of planar and tubular carbon. *Phys. Rev. Lett.* 84, 1716–1719. doi:10.1103/PhysRevLett.84.1716
- Tersoff, J. (1988). Empirical interatomic potential for carbon, with applications to amorphous carbon. *Phys. Rev. Lett.* 61, 2879–2882. doi:10.1103/PhysRevLett.61.2879
- Thompson, A. P., Aktulga, H. M., Berger, R., Bolintineanu, D. S., Brown, W. M., Crozier, P. S., et al. (2022). LAMMPS - a flexible simulation tool for particle-based materials modeling at the atomic, meso, and continuum scales. *Comput. Phys. Commun.* 271, 108171. doi:10.1016/j.cpc.2021.108171

- Tibbetts, G. G. (1984). Why are carbon filaments tubular? *J. Cryst. Growth* 66, 632–638. doi:10.1016/0022-0248(84)90163-5
- Tozzini, V., and Pellegrini, V. (2011). Reversible hydrogen storage by controlled buckling of graphene layers. *J. Phys. Chem. C* 115, 25523–25528. doi:10.1021/jp208262r
- Troiani, H. E., Miki-Yoshida, M., Camacho-Bragado, G. A., Marques, M. A. L., Rubio, A., Ascencio, J. A., et al. (2003). Direct observation of the mechanical properties of single-walled carbon nanotubes and their junctions at the atomic level. *Nano Lett.* 3, 751–755. doi:10.1021/nl0341640
- van Duin, A. C. T., Dasgupta, S., Lorant, F., and Goddard, W. A. (2001). Reaxff: A reactive force field for hydrocarbons. *J. Phys. Chem. A* 105, 9396–9409. doi:10.1021/jp004368u
- Walters, D. A., Ericson, L. M., Casavant, M. J., Liu, J., Colbert, D. T., Smith, K. A., et al. (1999). Elastic strain of freely suspended single-wall carbon nanotube ropes. *Appl. Phys. Lett.* 74, 3803–3805. doi:10.1063/1.124185
- Weiner, S. J., Kollman, P. A., Case, D. A., Singh, U. C., Ghio, C., Alagona, G., et al. (1984). A new force field for molecular mechanical simulation of nucleic acids and proteins. *J. Am. Chem. Soc.* 106, 765–784. doi:10.1021/ja00315a051
- Weiner, S. J., Kollman, P. A., Nguyen, D. T., and Case, D. A. (1986). An all atom force field for simulations of proteins and nucleic acids. *J. Comput. Chem.* 7, 230–252. doi:10.1002/jcc.540070216
- Wirz, L. N., Tonner, R., Hermann, A., Sure, R., and Schwerdtfeger, P. (2016). From small fullerenes to the graphene limit: A harmonic force-field method for fullerenes and a comparison to density functional calculations for goldberg–coxeter fullerenes up to c980. *J. Comput. Chem.* 37, 10–17. doi:10.1002/jcc.23894
- Yu, M.-F., Files, B. S., Arepalli, S., and Ruoff, R. S. (2000). Tensile loading of ropes of single wall carbon nanotubes and their mechanical properties. *Phys. Rev. Lett.* 84, 5552–5555. doi:10.1103/PhysRevLett.84.5552
- Zhao, X., Zhang, Y., Li, Y., and Liu, W. (2019). Molecular dynamics simulation of shear deformation of multi-layer graphene sheets with tersoff potential. *Int. J. Nanomanuf.* 15, 12–24. doi:10.1504/IJNM.2019.097235
- Zhu, Z., Fthenakis, Z. G., Guan, J., and Tománek, D. (2014). Topologically protected conduction state at carbon foam surfaces: An *ab initio* study. *Phys. Rev. Lett.* 112, 026803. doi:10.1103/PhysRevLett.112.026803